Cohesive fracture of plane orthotropic layers

Chien M. Nguyen [a], Alan J. Levy [b,*]

[a] National Heart, Lung and Blood Institute, National Institutes of Health, 5635 Fishers Lane, MSC 9314, Suite T-900, Bethesda, MD 20892-9314, United States
[b] Department of Mechanical and Aerospace Engineering, Syracuse University, Syracuse, NY 13244-1240, United States

ARTICLE INFO

ABSTRACT

Crack-like cohesive defect propagation within a plane orthotropic linear elastic layer is considered by assuming that the defect, and its growth under load, can be modeled as the evolving separation along a straight, predetermined nonlinear, nonuniform Needleman-type cohesive interface. The analysis exploits a general form of orthotropy rescaling originally developed for the displacement boundary value problem by Krenk (1979). It is shown that when the material is *degenerate orthotropic* (i.e., $\rho = 1$, ρ is the orthotropic shear parameter) rescaling enables the determination of solutions from isotropic ones and, when the material is fully orthotropic, rescaling allows for solutions to be obtained from problems with the simpler cubic symmetry. (These are well known attributes of linear *static sharp crack* analysis, which depend on an alternative form of rescaling the traction boundary value problem (Suo, 1990; Suo et al, 1991).) The procedure is demonstrated by obtaining degenerate orthotropic response from isotropic solutions recently obtained by the authors in an investigation of both solitary as well as multiple cohesive defect interaction problems in layered systems under arbitrary loading (Nguyen and Levy, 2009, 2011). In order to obtain fully orthotropic solutions via rescaling, a novel integral equation formulation is developed based on exact infinitesimal strain elasticity solutions for rectangular domains composed of cubically symmetric media and subject to arbitrary loading. Explicit results are obtained for the simple edge notch bend configuration, chosen so as to shed light on the mechanisms of defect propagation in orthotropic layers. It is demonstrated that increasing the orthotropic stiffness ratio can precipitate a quasi-brittle defect growth response. Furthermore, it is well known that in a number of technically important problem geometries and loadings, static sharp crack solutions are only weakly dependent on shear parameter ρ enabling the estimation of fully orthotropic behavior from isotropic solutions (Suo et al, 1991). This result is shown to be true for nonlinear cohesive fracture analysis of the edge notch bend configuration analyzed in this study.

1. Introduction

The purpose of this paper is to extend an exact theory of nonlinear cohesive fracture of isotropic planar layers (Nguyen and Levy, 2009, 2011) to the realm of orthotropic elasticity. The technical significance of the work stems from the widespread use of composite layers, at least one of which is anisotropic, in adhesive and protective coatings (Chvedov and Jones, 2004; Graziano, 2000; Boelen et al. 2004), in dental restorations consisting of ceramic, ceramic filled polymer and cementitious layers (Niu et al, 2008) and in the rehabilitation of structures where fiber reinforced plastic plate is adhered to damaged concrete beams (Carpinteri et al, 2007; Wang, 2007; Au and Buyukozturk, 2006; Pan and Leung, 2007; Rabinovitch, 2008). Numerous other applications exist as well. The subject of this paper is cohesive fracture within a *single* orthotropic layer exclusively, while future work will address the

heterogeneous multilayer cohesive interface fracture problem. The present analysis requires a straight nonlinear, nonuniform cohesive interface, along which a *crack-like defect*[1] will evolve, to be preselected to reside between two materially identical orthotropic sub-layers. Note that by nonlinear, nonuniform cohesive interface we mean an interface characterized by a traction-separation/slip relation that is a vector valued expression generally dependent on an interface coordinate dependent displacement jump vector and explicitly dependent on the interface coordinate through the interface strength. A well known example is the nonlinear exponential force law (Ferrante et al., 1982), which concerns normal separation only; given by $\mathbf{s}(\mathbf{n};v) = e\sigma_{\max}\frac{v}{\delta}e^{-v/\delta}\mathbf{n}$ where $\mathbf{s}$ is the traction vector on a side of the interface with unit normal $\mathbf{n}$ and v is the (normalized) normal component of displacement jump across the interface, generally dependent on an interface coordinate. The interface constitutive quantities $\sigma_{\max}$, δ characterize the interface

---

* Corresponding author. Tel.: +1 315 443 4365; fax: +1 315 433 9099.
   E-mail address: ajlevy@syr.edu (A.J. Levy).

[1] The term *crack* is reserved for the static sharp crack of fracture mechanics.

strength and the dimensionless force length, respectively. Interface nonuniformities including crack-like defects are considered by allowing the interface strength to be a function of interface coordinate x, i.e., $\sigma_{max}(x)$ (Needleman, 1990a; Needleman 1990b).

The approach taken here for the analysis of the orthotropic cohesive fracture problem is similar in some respects to one that is used in the well developed theory of *static sharp cracks* in plane rectangular anisotropic media in general, and orthotropic media in particular. In these problems, stress intensity factors for straight cracks in a variety of geometrical and loading configurations can be obtained by means of orthotropy rescaling of the governing orthotropic elasticity equations resulting in problems with cubic symmetry or, isotropic symmetry (provided the unscaled problem is *degenerate orthotropic*, i.e., $\rho = 1$, ρ is the orthotropic shear parameter (Suo, 1990; Suo et al, 1991)). The argument follows that, because many problems of technical interest have been solved for the simpler symmetry classes, their solutions can be exploited to yield the desired fully orthotropic (or degenerate orthotropic) solutions without much additional effort. Although the essence of the nonlinear cohesive fracture problem is fundamentally different from that of the linear static sharp crack, the overall philosophy employed here is the same as that used in Suo (1990), Suo et al (1991) to treat sharp cracks, i.e., to employ a rescaling of the equations to extract solutions for orthotropic media from isotropic or cubic media. Because the cohesive fracture problem, in contrast to the sharp crack problem, involves a nonlinear displacement boundary condition, the general form of rescaling introduced by Krenk (1979) will be employed. For problems with degenerate orthotropy, it is shown that rescaling reduces the problem to isotropic symmetry while fully orthotropic problems are reduced to problems with cubic symmetry. In the former case, isotropic solutions obtained by Nguyen and Levy (2009, 2011) are used to directly obtain orthotropic response via rescaling. In the later case an exact methodology, based on elasticity solutions for problems of cubic symmetry, is developed for loading consisting of pointwise prescribed strong boundary conditions on the upper and lower layer surfaces, and resultant prescribed weak boundary conditions on the side surfaces. This system models cohesive fracture in a single layer under a wide range of loading conditions. In particular, the stress function equation is solved in two sub layers adhered to each other along a cohesive interface and exact elasticity solutions for the boundary displacement components are written for each sub-layer. These are then pieced together to form integral equations governing displacement discontinuity components normal and tangent to the interface. The equations are necessarily nonlinear owing to nonlinear interface traction-separation/slip relations required to characterize the interface. The solution process proceeds by using eigenfunction expansion methods to reduce the integral equations to an infinite set of nonlinear algebraic equations which are then truncated and solved numerically.

In the next section (Section 2) orthotropy rescaling of the elasticity equations is discussed and extended to include the nonlinear cohesive interface boundary condition. Two problems involving degenerate orthotropic media are then solved by a rescaling of isotropic solutions obtained previously by the authors (Nguyen and Levy, 2009, 2011). The first problem deals with a cohesive defect (nonuniformity in interface strength) in a layer for which there is symmetry about the defect line (Fig. 1), while the second deals with a problem of stability of interfacial separation in a trilayer system (Fig. 5). Because fully orthotropic solutions can be obtained from cubic symmetry solutions, Section 3 presents an exact general theory of nonlinear cohesive defect growth in a layer composed of cubically symmetric media. Explicit results, including a discussion of the issue of ρ dependence, are presented for an edge notch bend configuration. The section closes with a demonstration of the remarkable fact that, for this configuration, increasing the

orthotropic stiffness ratio can precipitate a transition from more or less ductile defect growth to a quasi-brittle type of response characterized by an abrupt jump in defect length. The final section (Section 4) summarizes the findings and suggests further extensions of the work.

2. Orthotropy rescaling; degenerate orthotropic solutions

2.1. Displacement boundary value problem

Hooke's law for plane orthotropic linear elastic media assumes the form (Lekhnitskii, 1981),

$$e_i = \beta_{ij} t_j, \quad i, j = 1, 2, 6 \tag{1}$$

where the strain components e_i, $i = 1, 2, 6$ are given in terms of the strain tensor components by $[e_1, e_2, e_6]^T = [\varepsilon_{xx}, \varepsilon_{yy}, 2\varepsilon_{xy}]^T$ and the stress components t_i, $i = 1, 2, 6$ are given in terms of the stress tensor components by $[t_1, t_2, t_6]^T = [\sigma_{xx}, \sigma_{yy}, \sigma_{xy}]^T$. The coefficients β_{ij}, $i, j = 1, 2, 6$ have different forms depending on whether one is dealing with plane strain or plane stress. The coefficients β_{ij}, $i, j = 1, 2, 6$ have different forms depending on whether one is dealing with plane strain or plane stress. Thus, if $\beta_{ij} = \alpha_{ij}$, $i, j = 1, 2, 6$ are plane stress components, then the plane strain components are given by $\beta_{ij} = \alpha_{ij} - \alpha_{i3}\alpha_{j3}/\alpha_{33}$, $i, j = 1, 2, 6$. In terms of engineering moduli the α_{ij} are defined by, $\alpha_{11} = 1/E_1$, $\alpha_{22} = 1/E_2$, $\alpha_{12} = -\upsilon_{21}/E_2$, $\alpha_{21} = -\upsilon_{12}/E_1$, $\alpha_{66} = 1/G$ and $\alpha_{13} = -\upsilon_{31}/E_3$, $\alpha_{23} = -\upsilon_{32}/E_3$, $\alpha_{33} = 1/E_3$ with $\alpha_{12} = \alpha_{21} = -\upsilon_{21}/E_2 = -\upsilon_{12}/E_1$ (all other coefficients zero). The quantities (E_1, E_2, E_3) are stiffnesses, G is the in-plane shear modulus, and $(\upsilon_{12}, \upsilon_{21}, \upsilon_{13}, \upsilon_{31}, \upsilon_{23}, \upsilon_{32})$ are Poisson ratios, i.e., υ_{ij} characterizes the contraction in the j direction due to an extension in the i direction. There are four independent constants, i.e., five constants ($\beta_{11}, \beta_{22}, \beta_{12}, \beta_{21}, \beta_{66}$) connected by one constraint $\beta_{12} = \beta_{21}$. Following Krenk (1979) introduce quantities valid for both plane stress and plane strain: the *effective stiffness E*, the *effective Poisson ratio* υ, the *shear parameter* ρ and the *stiffness ratio* λ,[2]

$$E = \sqrt[-1]{\beta_{11}\beta_{22}}, \quad \upsilon = \sqrt{\frac{\beta_{12}\beta_{21}}{\beta_{11}\beta_{22}}}, \quad \rho = \frac{1}{2}\frac{2\beta_{12} + \beta_{66}}{\sqrt{\beta_{11}\beta_{22}}}, \quad \lambda = \frac{\beta_{11}}{\beta_{22}} \tag{2}$$

It is well known that, for rectilinear anisotropic media, the equilibrium equations will be satisfied when the stress components are written in the form $\sigma_{xx} = \frac{\partial^2 \varphi}{\partial y^2}$, $\sigma_{yy} = \frac{\partial^2 \varphi}{\partial x^2}$, $\sigma_{xy} = -\frac{\partial^2 \varphi}{\partial x \partial y}$ and the compatibility equations will be satisfied when the stress function φ satisfies the differential equation $\frac{\partial^4 \varphi}{\partial x^4} + 2\rho\lambda^{1/2}\frac{\partial^4 \varphi}{\partial x^2 \partial y^2} + \lambda\frac{\partial^4 \varphi}{\partial y^4} = 0$ where λ, ρ are defined above (Lekhnitskii, 1981).

If a change of variables[3] (Krenk, 1979) is introduced according to,

$$\hat{x} = \lambda^{1/8}x, \quad \hat{y} = \lambda^{-1/8}y, \quad \hat{u}_x = \lambda^{-1/8}u_x, \quad \hat{u}_y = \lambda^{1/8}u_y,$$
$$\hat{\varepsilon}_{xx} = \lambda^{-1/4}\varepsilon_{xx}, \quad \hat{\varepsilon}_{yy} = \lambda^{1/4}\varepsilon_{yy}, \quad \hat{\varepsilon}_{xy} = \varepsilon_{xy}, \tag{3}$$
$$\hat{\sigma}_{xx} = \lambda^{1/4}\sigma_{xx}, \quad \hat{\sigma}_{yy} = \lambda^{-1/4}\sigma_{yy}, \quad \hat{\sigma}_{xy} = \sigma_{xy},$$

then the following standard relationships are true,

$$\hat{\sigma}_{xx} = \frac{\partial^2 \hat{\varphi}}{\partial \hat{y}^2}, \quad \hat{\sigma}_{yy} = \frac{\partial^2 \hat{\varphi}}{\partial \hat{x}^2}, \quad \hat{\sigma}_{xy} = -\frac{\partial^2 \hat{\varphi}}{\partial \hat{x} \partial \hat{y}},$$
$$\hat{\varepsilon}_{xx} = \frac{\partial \hat{u}_x}{\partial \hat{x}}, \quad \hat{\varepsilon}_{yy} = \frac{\partial \hat{u}_y}{\partial \hat{y}}, \quad 2\hat{\varepsilon}_{xy} = \frac{\partial \hat{u}_y}{\partial \hat{x}} + \frac{\partial \hat{u}_x}{\partial \hat{y}}. \tag{4}$$

The stress function $\hat{\varphi}$ now satisfies the rescaled equation,

$$\frac{\partial^4 \hat{\varphi}}{\partial \hat{x}^4} + 2\rho\frac{\partial^4 \hat{\varphi}}{\partial \hat{x}^2 \partial \hat{y}^2} + \frac{\partial^4 \hat{\varphi}}{\partial \hat{y}^4} = 0, \tag{5}$$

---

[2] For many materials of interest $0 < \rho < 5$, $1/20 < \lambda < 20$ (Bao et al, 1992).

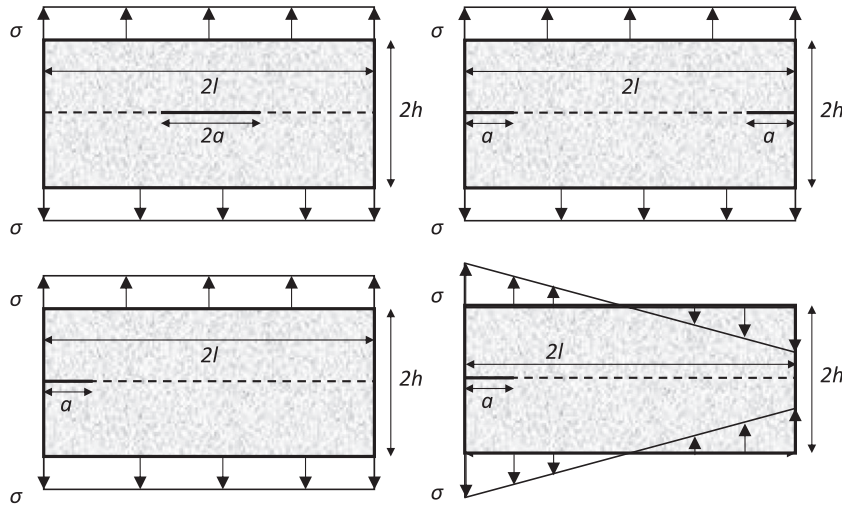[3] In what follows a caret will designate a scaled variable.

Fig. 1. Clockwise from upper left. (i) center crack, (ii) double edge notched, (iii) edge notched bend, (iv) single edge notched.

and, the stress strain relations assume the form,

$$\begin{bmatrix} \hat{\varepsilon}_{xx} \\ \hat{\varepsilon}_{yy} \\ 2\hat{\varepsilon}_{xy} \end{bmatrix} = \frac{1}{E}\begin{pmatrix} 1 & -\upsilon & 0 \\ -\upsilon & 1 & 0 \\ 0 & 0 & 2(\rho+\upsilon) \end{pmatrix}\begin{bmatrix} \hat{\sigma}_{xx} \\ \hat{\sigma}_{yy} \\ \hat{\sigma}_{xy} \end{bmatrix} \quad (6)$$

Thus, both orthotropic plane stress and plane strain constitutive relations, when expressed in rescaled variables (3), assume the plane stress form (6) for materials with cubic symmetry provided the effective material constants (E, υ, ρ) take on the appropriate values through the definitions for the β_{ij} coefficients (see (1) and (2)).

2.2. Decohesive interface boundary condition

The particular problems of interest in this work involve the analysis of *crack-like cohesive defect* growth by the evolving separation/extension along a preselected interface. This requires a boundary condition that has a nonlinear coupling of the normal or shear interface traction components to the normal and tangential displacement jump components. In order to model preexisting defects, these relations also depend functionally on an interface coordinate. To see how the change of variables (3) effect nonlinear interface force laws assume that interface traction components along a straight interface y = 0 (in unscaled variables) are of the form $\tau_{\max}(x)f_x(u/\delta_t, v/\delta_n)$, $\sigma_{\max}(x)f_y(u/\delta_t, v/\delta_n)$ where $\tau_{\max}(\sigma_{\max})$ is the interface strength in shear(normal) mode and $f_x(f_y)$ are nondimensional shear(normal) traction components equal to the stress components on one side of the interface,

$$\sigma_{xy}(x,y=0) = \tau_{\max}(x)f_x\left(\frac{u}{\delta_t},\frac{v}{\delta_n}\right),$$

$$\sigma_{yy}(x,y=0) = \sigma_{\max}(x)f_y\left(\frac{u}{\delta_t},\frac{v}{\delta_n}\right). \quad (7)$$

The interface force representation (7) is general enough to accommodate many force laws currently in use including the uncoupled piecewise linear model and the Xu–Needleman law used below. (In the latter, f_y depends on a "q" coupling parameter, the ratio of shear interface energy to normal interface energy for complete separation, which remains unchanged in the rescaling process, i.e., $\frac{\hat{\tau}_{\max}\hat{\delta}_t}{\hat{\sigma}_{\max}\hat{\delta}_n} = \frac{\tau_{\max}\delta_t}{\sigma_{\max}\delta_n}$. This follows from (8) and (9) below.) In (7), x is now the normalized interface coordinate and u, v the normalized displacement jump components tangent and normal to the interface, respectively defined by $lu = [u_x] =$

$Limu_x(x,y\downarrow 0) - Limu_x(x,y\uparrow 0)$, $lv = [u_y] = Limu_y(x,y\downarrow 0) - Limu_y(x,y\uparrow 0)$ and δ_t, δ_n are the interface force length constitutive constants in shear and normal mode, respectively. Quantities x, u, v, δ_n, δ_t are normalized by the characteristic dimension l (for example the layer half length) along the x axis so that in terms of scaled variables,

$$\hat{v} = v, \quad \hat{u} = \lambda^{-1/4}u, \quad \hat{\delta}_n = \delta_n, \quad \hat{\delta}_t = \lambda^{-1/4}\delta_t, \quad \hat{l} = \lambda^{1/8}l \quad (8)$$

where use has been made of (3). The interface traction components become,

$$\hat{\sigma}_{xy}(\hat{x},\hat{y}=0) = \hat{\tau}_{\max}(\hat{x})f_x(\hat{u}/\hat{\delta}_t, \hat{v}/\hat{\delta}_n),$$

$$\hat{\sigma}_{yy}(\hat{x},\hat{y}=0) = \hat{\sigma}_{\max}(\hat{x})f_y(\hat{u}/\hat{\delta}_t, \hat{v}/\hat{\delta}_n),$$

with $\hat{\tau}_{\max} = \tau_{\max}$,

$$\hat{\sigma}_{\max} = \lambda^{-1/4}\sigma_{\max} \quad (9)$$

For interface force laws of the form (7), the *work of separation* in normal mode (ϕ_n) and the *initial interface stiffness* (κ_n) are defined by,

$$\phi_n = \sigma_{\max}\int_0^\infty f_y(0,v/\delta_n)d(lv) = (l\delta_n)\sigma_{\max}\tau_1, \quad \tau_1 = \int_0^\infty f_y(0,\xi)d\xi$$

$$\kappa_n = \sigma_{\max}(l\delta_n)^{-1}D_2f_y(0,\xi)\big|_{\xi=0} = (l\delta_n)^{-1}\sigma_{\max}\tau_2, \quad \tau_2 = D_2f_y(0,\xi)\big|_{\xi=0} \quad (10)$$

where $l\delta_n$ is the dimensioned force length in normal mode and $D_2f_y(0,\xi)\big|_{\xi=0}$ means *take the derivative of f_y with respect to its second argument ξ and then substitute $\xi = 0$*. In rescaled variables (8)–(10) imply,

$$\hat{\phi}_n = \lambda^{-1/8}\phi_n,$$

$$\hat{\kappa}_n = \lambda^{-3/8}\kappa_n \quad (11)$$

As an example consider the physically based nonlinear exponential force law for normal mode (Ferrante et al, 1982) given by,

$$\sigma_{yy}(x,y=0) = \sigma_{\max}f_y(v/\delta_n),$$

$$f_y(v/\delta_n) = e\frac{v}{\delta_n}e^{-v/\delta_n} \quad (12)$$

where $\sigma_{\max}$ is constant. In normal mode the work of separation is given by $\phi_n = e(l\delta_n)\sigma_{\max}$ while the initial interface stiffness is given by $\kappa_n = e(l\delta_n)^{-1}\sigma_{\max}$. In rescaled variables the boundary condition assumes the form $\hat{\sigma}_{yy}(\hat{x},\hat{y}=0) = e\hat{\sigma}_{\max}\frac{\hat{v}}{\hat{\delta}_n}e^{-\hat{v}/\hat{\delta}_n}$.

Note that in all of the calculations that follow we use the smooth hyperelastic exponential interface force law proposed by

Xu and Needleman (1993) which couples the physically based nonlinear normal force-separation relation (12) to a phenomenological nonlinear shear mechanism. This model allows for both normal and shear failure modes along the interface and was originally derived for sharp, crystalline interfaces. It is used here because it is general enough to capture most of the physically reasonable interactions between the normal and shear modes. Although certain anomalies are known to exist with the Xu–Needleman force law improvements/modifications are not without their own limitations (Van den Bosch et al., 2006). For an up-to-date review of interface models, some of which include a wider range of interface behavior such as coupled adhesion, friction and viscous dissipation under monotonic and cyclic loading, see Raous (2011). Here we will use the Xu–Needleman law in its original form. In Nguyen and Levy (2009) the Xu–Needleman law was compared with an uncoupled piecewise linear law in an isotropic bilayer system. The results were qualitatively the same although the Xu–Needleman law gave a slightly stiffer response. Because many previous studies have expounded at length on the features of this particular force law we only note here that there are four interfacial constitutive parameters[4]: normal characteristic force length (δ_n) normalized by layer half-length (l), the normal interface strength ($\sigma_{\max}$), the ratio of shear interface energy to normal interface energy for complete separation ($q = \phi_t/\phi_n$), and the shear stiffness/strength parameter Γ. Another equivalent set is: normal characteristic force length (δ_n), the normal interface strength ($\sigma_{\max}$), the shear characteristic force length (δ_t) (defined by $\delta_t = \Gamma^{-1}\delta_n$), the shear interface strength ($\tau_{\max}$) (defined by $\tau_{\max} = q\Gamma\sigma_{\max}\sqrt{2e}$) where the first (last) two characterize normal (shear) mode response. Furthermore, from (10), the normal (shear) energy of complete separation is given by $\phi_n = (l\delta_n)\sigma_{\max}e^1$, ($\phi_t = (l\delta_t)\tau_{\max}\sqrt{e/2}$) with $\phi_t = q\phi_n$. The initial normal stiffness is $\kappa_n = (l\delta_n)^{-1}\sigma_{\max}e$ while the initial shear stiffness is $\kappa_t = (l\delta_t)^{-1}\tau_{\max}\sqrt{2e}$. The uncoupled normal and tangential interface constitutive relations $f_y(0, v)$ and $f_x(u, 0)$ are shown in Fig. 2 for different interface characteristic force lengths δ_n and δ_t, respectively. Note that the parameter values $q = 0.5$, $\Gamma = 0.7$ are used in all calculations reflecting an interface that is weaker and more ductile ($\tau_{\max} = .816\sigma_{\max}$, $\delta_t = 1.43\delta_n$, $\phi_t = 0.5\phi_n$), and initially more compliant, in shear ($\kappa_t \approx \frac{1}{2}\kappa_n$).

The rescaled problem defined by (4), (5), (6), and (9) involves only three bulk material parameters (E, v, ρ) and is formally equivalent to problems concerning materials with cubic symmetry. Note that if $\rho = 1$, the so called *degenerate* class of orthotropic materials (Suo et al, 1991), the rescaled constitutive relation (6) is of isotropic form and depends on only two bulk material parameters (E, v). For many orthotropic traction boundary value problems involving static sharp cracks the solutions are insensitive to ρ. This feature enables the estimation of stress intensity factors for fully orthotropic media from isotropic ones via rescaling. One of the purposes of this paper is to investigate whether this attribute might hold for nonlinear cohesive fracture analysis. (This will be considered in a later section.) The following two problems are concerned with the determination of degenerate orthotropic behavior from isotropic solutions obtained in previous work (Nguyen and Levy, 2009, 2011).

2.3. A cohesive defect in an orthotropic plate

Consider a cohesive defect in an isotropic plate in plane stress, situated along the *x*-axis and opened in such a way that there is no shear along the defect line. In this problem the cohesive defect
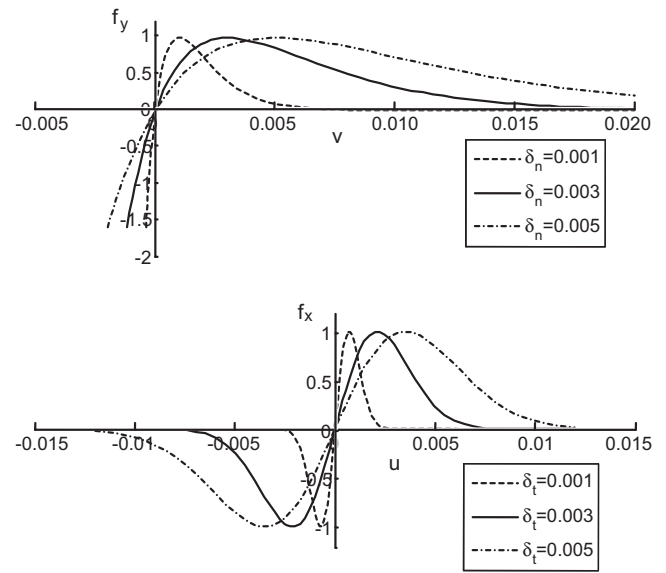

Fig. 2. Interface force law in normal and shear mode.

is taken in the form of an interface coordinate dependent interface strength given by,

$$\sigma_{\max}(x) = \begin{cases} \sigma_{\max}^0, & |x| > a \\ \sigma_{\max}^0 - p, & |x| \leqslant a \end{cases} \tag{13}$$

where $\sigma_{\max}^0$ is constant. (Note that the *crack-like defect* approximation to the *static sharp crack* can be obtained by letting $p = \sigma_{\max}^0$). Four such configurations have been considered for the *static sharp crack* in Bao et al (1992), i.e., the center crack (CC), the single edged notch (SEN), the double edged notch (DEN) and the edge notch bend (ENB) configurations (Fig. 1). For cohesive defects in these configurations, the normal component of displacement jump along the entire cohesive interface can be written as,

$$\hat{v} = H\left(\hat{x}, \hat{a}, \frac{\hat{\sigma}}{E}, \frac{\sigma_{\max}^0}{E}, \hat{\delta}_n, v\right) \tag{14}$$

where $\hat{a}$ (normalized by $\hat{l}$) is the defect or half-defect length depending on the particular defect configuration. The function H can be found in numerical or graphical form by the methods described in Nguyen and Levy (2009, 2011). Rescaling the variables according to (3) and (8) leads to,

$$v = H\left(x, a, \frac{\sigma}{\lambda^{1/4}E}, \frac{\sigma_{\max}^0}{\lambda^{1/4}E}, \delta_n, v\right) \tag{15}$$

where E, v are now regarded as effective orthotropic moduli in the sense of (2). Thus, degenerate orthotropic response is obtained by letting,

$$E \to \lambda^{1/4}E = \lambda^{1/4}(\beta_{11}\beta_{22})^{-1/2}, \quad v \to \sqrt{\frac{\beta_{12}\beta_{21}}{\beta_{11}\beta_{22}}} \tag{16}$$

in the isotropic solution. Note that $\hat{v}$ may depend on $\hat{h}/\hat{l}$ as well and if this ratio is small the replacement scheme will also involve $\hat{h}/\hat{l} \to \lambda^{-1/4}h/l$. In the case of a fiber composite where the (stiffer) fibers are oriented in the *x* direction $E_1 > E_2$ and $\lambda < 1$. The effective half length of the orthotropic plate $\lambda^{1/4}l$ is therefore less than its isotropic counterpart by a multiplicative factor of $\lambda^{1/4}$. This phenomenon has been termed $\lambda^{1/4}$ contraction by Suo et al (1991) and has implications in choosing the proper lengths of orthotropic test specimens in order to minimize end effects. For the case of a cohesive defect (15) indicates that the effective stiffness E, defined in (2),

undergoes an analogous $\lambda^{1/4}$ *stiffness contraction* To see this, compare the response of a degenerate orthotropic layer with that of an isotropic layer for the case where they both have identical defect geometry ($a = \hat{a}$), loading ($\sigma = \hat{\sigma}$), interface constitutive constants ($\sigma^0_{\max} = \hat{\sigma}^0_{\max}$, $\delta_n = \hat{\delta}_n$) and bulk constitutive constants (E, υ) such that the isotropic stiffness and Poisson ratio are the same as their effective orthotropic counterparts as given by (2). Under these conditions (14) and (15) indicate different separation behaviors determined by the stiffness ratio λ.

The traction component along the entire cohesive interface is given by (9)$_2$,

$$\frac{\hat{\sigma}_{yy}}{\hat{\sigma}} = \frac{\hat{\sigma}_{\max}(\hat{x}, \hat{a})}{\hat{\sigma}} f_y(\hat{\upsilon}/\hat{\delta}_n) \tag{17}$$

which in rescaled variables is of identical form provided the carets are removed. Thus, σ_{yy} is obtained from $\hat{\sigma}_{yy}$ by the same replacement scheme as that of υ. When comparing degenerate orthotropic response to that of an isotropic layer of similar properties it was found that the separation υ changed with stiffness ratio λ. This same behavior can be expected of σ_{yy} as well given (17). By judicious choice of constitutive coefficients the above analysis can be used to obtain an approximation of *static sharp crack* behavior (this has been done in Nguyen and Levy (2011) for isotropic response of a layer with *center crack* geometry). In particular, $p = \sigma^0_{\max}$ in (13), the remote tensile loading $\hat{\sigma}$ is assumed less than the interface strength $\hat{\sigma}^0_{\max}$ (which is taken to equal the elastic modulus E), and the elastic modulus is assumed less than the initial interface stiffness, i.e., $\hat{\sigma} < \hat{\sigma}^0_{\max}/100 < \hat{\sigma}^0_{\max} = E < e\hat{\sigma}^0_{\max}/\hat{\delta}_n$ where $e\hat{\sigma}^0_{\max}/\hat{\delta}_n$ is the normalized initial interface stiffness in normal mode. It can be shown that under these assumptions rescaling leads to an interface separation behind the defect tip given by,

$$\upsilon = \frac{\lambda^{-1/4}\sigma}{E} \mathscr{H}(x, a) \tag{18}$$

and a normal component of traction ahead of the defect tip given by,

$$\sigma_{yy}(x, a) = \sigma \mathscr{K}(x, a) \tag{19}$$

which is independent of stiffness ratio λ. Note that (18) and (19) were obtained assuming that that the quantity $\lambda^{-1/4}h/l$ is large enough to be neglected. For the problem of a *sharp crack* in an isotropic plate in one of the four plane stress opening mode configurations (CC, SEN, DEN, DNB) solutions are well known (Bao et al, 1992). When these results are rescaled for degenerate orthotropic material behavior they assume the form of (18) and (19). Fig. 3 depicts the normalized traction (or stress concentration factor) along the defect line in the CC configuration (Fig. 1) for the *crack-like defect* of half length $a = 0.5$. Also plotted is the *static sharp crack* solution. All results have been rescaled from isotropic results (for the *sharp crack* we have used the Koiter and Benthem solution (Koiter and Benthem, 1973), while for the cohesive defect we have used the results of Nguyen and Levy (2011)). Note that different values of stiffness ratio λ give different values for E for an equivalent isotropic material. Curves for the *crack-like defect* are plotted for five different values of stiffness ratio λ. Note that these curves are generally independent of λ only when $\lambda^{-1/4}h/l > 2$ (Bao et al 1992) (this is the case for which the *sharp crack* solution has been plotted). For the values of h/l chosen, i.e., $h/l = 0.675$, the condition $\lambda^{-1/4}h/l > 2$ will be satisfied when $\lambda < 0.013$. Two of the five curves ($\lambda = 0.001, 0.01$) plotted in Fig. 3 satisfy this condition and indeed coalesce with each other (and approximate the sharp crack solution which is λ independent). Recall that the classical fracture solution has a stress singularity at the crack tip and the normalized stress away from the crack tip decreases to values that are smaller than the nominal stress (for the crack length shown). This is because the *static sharp crack* solution is limited in that it applies only in

the neighborhood of the crack tip. The solutions for the *crack-like cohesive defect* presented here yield stress distributions that (i) have finite values at the defect tip (assumed to be located at the unloaded defect half length), (ii) have values that are valid along the entire length ($2l$ in Fig. 1) of the cohesive defect line (not just near the defect tip) and (iii) evolve nonlinearly with increasing load. The *crack like cohesive defect* solutions, at points far from the defect tip, becomes smaller than the nominal stress when the stiffness ratio λ increases (Fig. 3) and, in fact may become negative near the vertical boundary. This phenomenon is an effect of rescaling and the finite height h of the geometry on the normal stress component which cannot be captured in classical crack theories (i.e., $\lambda^{-1/4}h/l$ and increasing λ contracts h). Thus, for small $\lambda^{-1/4}h/l$ bending dominates over the direct action of the nominal stress giving rise to compressive regions ahead of the defect tips.

Fig. 4 depicts the distribution of normalized normal component of displacement jump υ at different values of stiffness ratio λ. Note that the curves are not consistent with what we would expect physically because they indicate that increasing λ (increasing ratio E_2/E_1) gives rise to a more compliant behavior. Furthermore this fact, that the response becomes more compliant under increasing λ, seems to contradict (18) which indicates a contrary response. This is due to the fact that in this calculation the rigid displacements of the top and bottom sublayers are controlled and not the nominal load. Thus, for the same rigid displacements, an increase in E_2 reduces the stretching of the sublayers in the nominal stress direction giving rise to an increase in υ. Note that the curves reveal very small separations of the interface in bonded zones and a short contact region at the ends of the interface that is consistent with the stress distribution in Fig. 3.

2.4. The stability of separation in a uniform trilayer system

Consider the following problem of the *uniform* separation of three layers bonded together along two interfaces characterized by uniform (constant $\hat{\sigma}_{\max}$) nonlinear traction-separation/slip relations (7). This problem is nontrivial owing to the fact that the middle layer will displace rigidly at some point in the deformation process while maintaining uniform separations above and below it. Assume the layers have identical, degenerate orthotropic material properties and that the outer two layers have the same thickness (Fig. 5). This problem was chosen for analysis because it allows the direct exploration of some of the features of orthotropic response by rescaling the exact nontrivial solutions to the isotropic version of the problem (Nguyen and Levy, 2011). In Nguyen and Levy (2011) the outer two layers were assumed identical, but *materially* and *geometrically* distinct from the middle layer. (This system is not considered here because the present form of rescaling does not readily allow for a meaningful definition of displacement jump across two materially distinct orthotropic layers.) The equations governing the solution to the isotropic plane stress problem are obtained from global equilibrium of the layers and, the nonlinear interface displacement/traction boundary condition between the layers,

$$\hat{\sigma} - f_y^1\left(\frac{\hat{\upsilon}^1}{\hat{\delta}_n}\right) = 0, \quad \hat{\sigma} - f_y^2\left(\frac{\hat{\upsilon}^2}{\hat{\delta}_n}\right) = 0,$$

$$\hat{\upsilon}^1 + \hat{\chi}f_y^1\left(\frac{\hat{\upsilon}^1}{\hat{\delta}_n}\right) - \hat{\upsilon}_R^1 + \hat{\upsilon}_R^2 = 0, \quad \hat{\upsilon}^2 + \hat{\chi}f_y^2\left(\frac{\hat{\upsilon}^2}{\hat{\delta}_n}\right) - \hat{\upsilon}_R^2 - \hat{\upsilon}_R^1 = 0, \tag{20}$$

where $\hat{\upsilon}^1$ ($\hat{\upsilon}^2$) are uniform separations of the first (second) interface,[5] $\hat{\upsilon}_R^1 (= -\hat{\upsilon}_R^3)$ is the prescribed rigid displacement of the upper layer (lower layer) and $\hat{\upsilon}_R^2$ is the rigid displacement of the middle
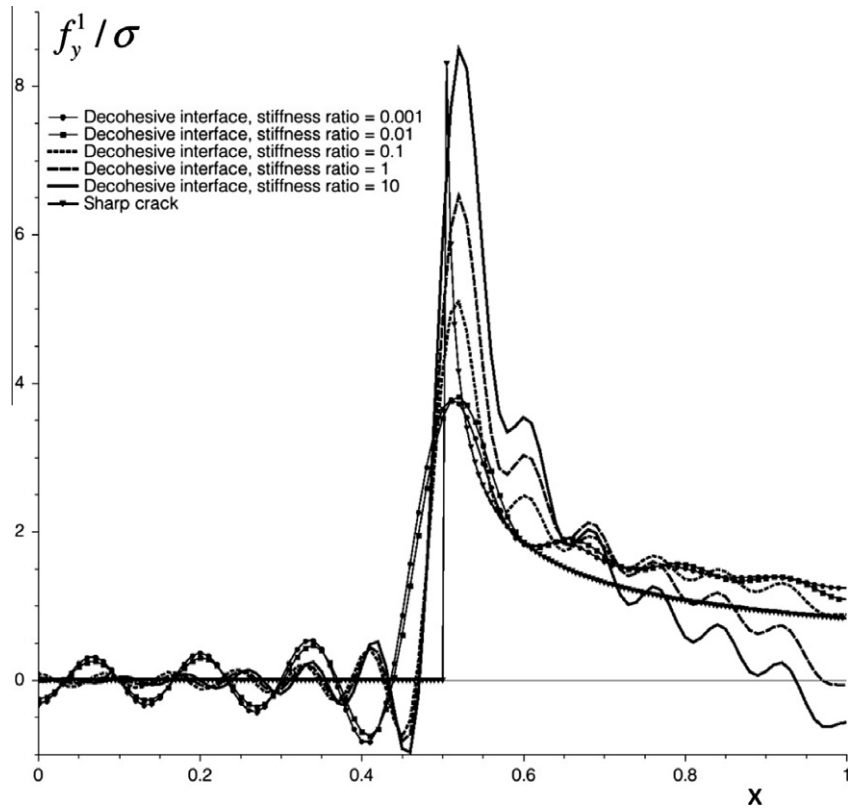
---

[5] Counted down from the top.

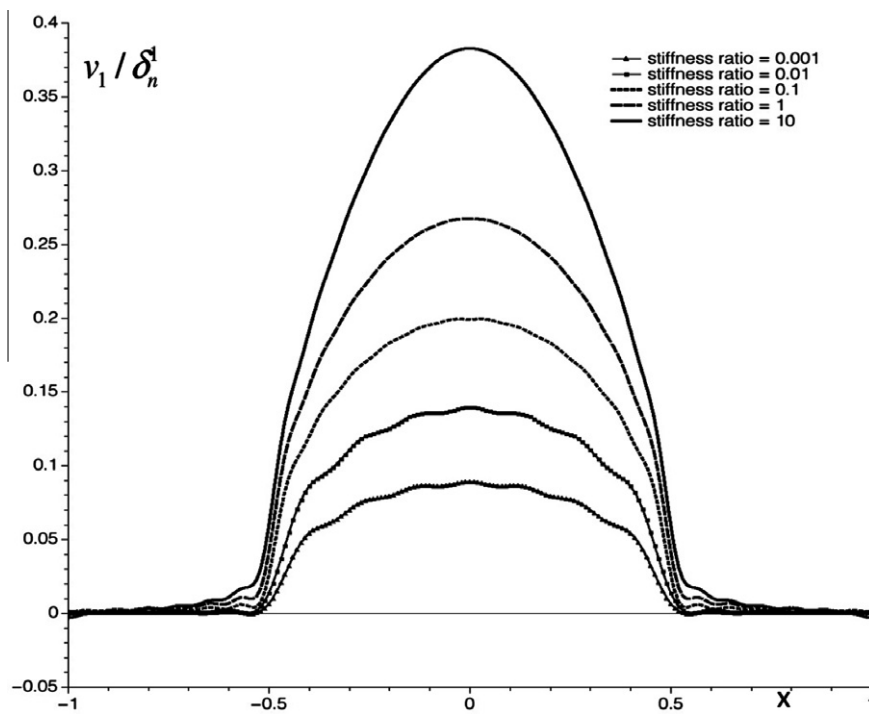**Fig. 3.** Distribution of normal traction. Center crack geometry; Degenerate orthotropy.

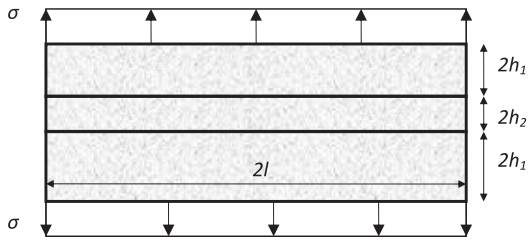**Fig. 4.** Distribution of normal separation for the cases in Fig. 3.

Fig. 5. The uniformly loaded materially uniform trilayer.

layer. Note that in this section the boundary traction $\hat{\sigma}$ is normalized by $\hat{\sigma}_{max}$ and is part of the solution. All displacement quantities in (20) are normalized by layer half length $\hat{l}$. In addition, the nondimensional parameter $\hat{\chi}$ is given by,

$$\hat{\chi} = \frac{\hat{\sigma}_{max}}{E}(\hat{\gamma}_1 + \hat{\gamma}_2) \qquad (21)$$

where $\hat{\gamma}_1, \hat{\gamma}_2$ are the normalized thicknesses of the first and second layers, e.g., $\hat{\gamma}_1 = \hat{h}_1/\hat{l}$. Note that interfacial separations above and below the middle layer $\hat{v}^1, \hat{v}^2$ are not necessarily the same because $(f_y)^{-1}$, for the force law (12), is multivalued. The solutions for $\hat{v}_R^2, \hat{\sigma}$ can be obtained from (12), (20)$_1$ and (20)$_2$ (once $\hat{v}^1, \hat{v}^2$ have been eliminated using (20)$_3$ and (20)$_4$). They are given implicitly by,

solution one : $\hat{v}_R^2 = 0, \hat{v}_R^1 - \hat{\chi}\hat{\sigma} + \hat{\delta}_n W_1(-\hat{\sigma}e^{-1}) = 0,$

solution two : $\hat{v}_R^2 + \frac{1}{2}\hat{\delta}_n[W_1(-\hat{\sigma}e^{-1}) - W_2(-\hat{\sigma}e^{-1})] = 0,$ 　(22)

$\hat{v}_R^1 - \hat{\chi}\hat{\sigma} + \frac{1}{2}\hat{\delta}_n[W_1(-\hat{\sigma}e^{-1}) + W_2(-\hat{\sigma}e^{-1})] = 0,$

where W_1, W_2 are real valued branches of the multivalued Lambert W function (recall that the solution to the equation $y \exp(y) = x$ is $y = W(x)$ and, as seen in Fig. 6, $W_1(x)$ is the principal branch with $W_1(0) = 0$ (Corless et al, 1996)). Note that the uniform separations $\hat{v}^1, \hat{v}^2$ then follow from (20)$_3$ and (20)$_4$. The global behavior of solutions (22) is summarized in Fig. 7 which depicts the rigid displacement of the middle layer as a function of rigid loading of top (and bottom) layer $\hat{v}_R^1(= -\hat{v}_R^3)$ for different values of parameter $\hat{\chi}\hat{\delta}_n^{-1}$.
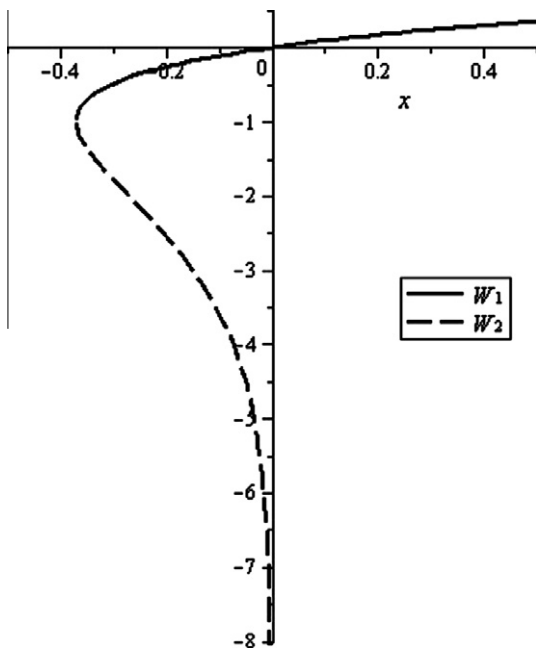

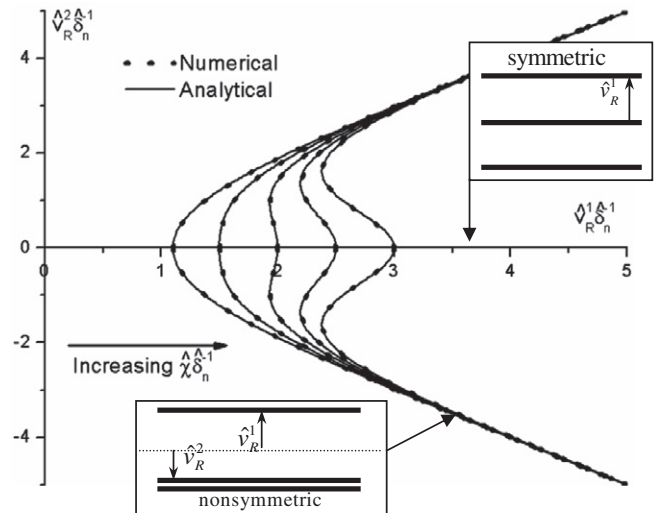**Fig. 6.** The real valued branches of the Lambert W function.

Fig. 7. The uniform mode solution. Displacement. $\hat{\chi}\hat{\delta}_n^{-1} = 0.1, 0.5, 1.0, 1.5, 2.0.$

The figure indicates that for values of $\hat{v}_R^1/\hat{\delta}_n$ less than a critical value $\hat{v}_{RC}^1/\hat{\delta}_n$ (which is greater than one) only the symmetric solution is available, i.e., one for which the centerline of the middle layer does not displace rigidly. For values of $\hat{v}_R^1/\hat{\delta}_n$, greater than critical $\hat{v}_{RC}^1/\hat{\delta}_n$, generally dependent on $\hat{\chi}\hat{\delta}_n^{-1}$, a second, nonsymmetric solution becomes available i.e., one for which the centerline of the middle layer displaces rigidly. The symmetric and nonsymmetric solutions are illustrated in the boxes in Fig. 7. It can be shown (Nguyen and Levy, 2011) that the critical value $\hat{v}_{RC}^1/\hat{\delta}_n$ is given by,

$$\hat{v}_{RC}^1 = \hat{\delta}_n + \hat{\chi} = \hat{\delta}_n + \frac{\hat{\sigma}_{max}}{E}(\hat{\gamma}_1 + \hat{\gamma}_2). \qquad (23)$$

Furthermore, the transition to the nonsymmetric branch can be gradual, for values of $\hat{\chi}\hat{\delta}_n^{-1} < 2/3$, or abrupt for values of $\hat{\chi}\hat{\delta}_n^{-1} > 2/3$. Thus, from (21), small force length parameter $\hat{\delta}_n$, large interface strength $\hat{\sigma}_{max}$, small effective stiffness E, and large thickness ratios $\hat{\gamma}_1 = \hat{h}_1/\hat{l}$, $\hat{\gamma}_2 = \hat{h}_2/\hat{l}$ favor abrupt or brittle nonsymmetric separation. As one moves from the origin along the positive $\hat{v}_R^1/\hat{\delta}_n$ axis in Fig. 7 the number of solutions increases from 1 (when $\hat{v}_R^1/\hat{\delta}_n < \hat{v}_{RC}^1/\hat{\delta}_n$) to 3 (when $\hat{v}_R^1/\hat{\delta}_n > \hat{v}_{RC}^1/\hat{\delta}_n$ and $\hat{\chi}\hat{\delta}_n^{-1} < 2/3$) to 5 (when $\hat{v}_R^1/\hat{\delta}_n > \hat{v}_{RC}^1/\hat{\delta}_n$ and $\hat{\chi}\hat{\delta}_n^{-1} > 2/3$). Because there is no bias in the system towards displacement above or below the horizontal, nonsymmetric solutions can be in the first or fourth quadrant. (For a discussion of the stability characteristics of the equilibrium branches see Nguyen and Levy (2011)).

The solution described above is for the plane stress isotropic problem or, by the rescaling procedure outlined above, for the plane degenerate orthotropic problem provided the careted quantities are rescaled. The transformation from rescaled variables to original variables can be affected through the transformation formulae (3) and (8) together with the relations $\hat{\tau}_{max} = \tau_{max}$, $\hat{\sigma}_{max} = \lambda^{-1/4}\sigma_{max}$. Thus,

$$\hat{\sigma} = \sigma, \quad \frac{\hat{v}^1}{\hat{\delta}_n} = \frac{v^1}{\delta_n}, \quad \hat{v}_R^1 = v_R^1, \quad \hat{v}_R^2 = v_R^2, \qquad (24)$$

where σ is the boundary loading normalized by σ_{max}, (σ_{max}, δ_n) are respectively the (constant) interface strength and the normalized (with respect to the layer half-length l) interface force length parameter. The quantities v^1, v_R^2, v_R^1 are the displacement jump, the rigid displacement of the middle layer and the controlled rigid displacement of the outer layers normalized by l. The parameter $\hat{\chi}$, defined by (21), in unscaled variables becomes,

$$\hat{\chi} = \frac{\hat{\sigma}_{max}}{E}(\hat{\gamma}_1 + \hat{\gamma}_2) = \lambda^{-1/2}\frac{\sigma_{max}}{E}(\gamma_1 + \gamma_2) = \lambda^{-1/2}\chi$$
$$= \beta_{22}\sigma_{max}(\gamma_1 + \gamma_2), \tag{25}$$

where use has been made of (2) and the following,

$$\hat{\gamma}_1 = \frac{\hat{h}_1}{\hat{l}} = \frac{\lambda^{-1/8}h_1}{\lambda^{1/8}l} = \lambda^{-1/4}\frac{h_1}{l} = \lambda^{-1/4}\gamma_1, \quad \hat{\gamma}_2 = \lambda^{-1/4}\gamma_2, \tag{26}$$
$$\hat{\sigma}_{max} = \lambda^{-1/4}\sigma_{max}$$

A direct analysis of the general orthotropic equations (4)–(6) and (12)$_1$ reveals that governing equations are identical in form to (20) which were obtained by rescaling of the isotropic equations. Note that for this problem, both the nondegenerate ($\rho \neq 1$) and the degenerate ($\rho = 1$) orthotropic equations are the same because they are independent of shear parameter ρ. Thus, the solution (22) (for force law (12)$_2$), and the critical rigid separation (23) apply to both the nondegenerate ($\rho \neq 1$) and the degenerate ($\rho = 1$) ortho-tropic problems provided $\hat{\chi} = \beta_{22}\sigma_{max}(\gamma_1 + \gamma_2)$. Because the impact of orthotropy is felt solely through the parameter $\hat{\chi}$ this allows for a simple interpretation of behavior based on the non-dimensional-ized isotropic solution (Fig. 7). Note that this feature is independent of the particular form of force law provided it can be written in the form $\sigma_{max}f_y(v/\delta_n)$.

It is interesting to note that for plane stress $\beta_{22} = 1/E_2$, so the problem is formally equivalent to the isotropic problem with iso-tropic stiffness E replaced by directional stiffness E_2. For plane strain $\beta_{22} = 1/E_2 - v_{32}^2/E_3$ and, because a nonzero stress σ_{zz} is in-duced owing to the plane strain constraint ($\varepsilon_{zz} = 0$), the response will depend on the stiffnesses in both y and z directions. In order to explore this behavior consider transversely isotropic response arising from a randomly arrayed unidirectional fiber reinforced composite layer in which the fibers are much stiffer than the ma-trix. Consider two different configurations, one in which the fibers are oriented along the x axis and another in which the fibers are oriented along the z axis. In both cases the rigid separation applied to the layers is perpendicular to the fiber direction. In the first case however $E_2 = E_3 < E_1$, while in the second case $E_1 = E_2 < E_3$. The above considerations indicate identical response in both cases for plane stress ($\beta_{22} = 1/E_2$) governed essentially by the stiffness of the matrix. In contrast to plane stress, plane strain gives markedly different response for the two fiber configurations. In the first case ($E_2 = E_3 < E_1$) and $\beta_{22} = (1 - v_{32}^2)/E_2$ which is equivalent to isotropic response in the y, z plane. In the second case, $E_1 = E_2 < E_3$ so that $\beta_{22} = 1/E_2$ (in the limit of infinitely stiff fibers). In this case β_{22} is larger (the response is more compliant in the y direction) and, by (25) $\hat{\chi}$ is larger as well. The consequences for behavior are indi-cated in Fig. 7, i.e., a delayed transition to unstable behavior but a tendency towards more brittle response.

3. Problems with cubic material symmetry; ρ dependence

3.1. General theory

The general theory for materials with cubic symmetry follows along the lines of Nguyen and Levy (2009) for isotropic materials. Note that in this subsection all field variables are unscaled and ap-ply to problems with cubic symmetry. Application to the fully orthotropic problem by means of rescaling will be carried out in a later subsection. Consider a plane linear elastic sublayer $B = \{(x,y)|x \in (-l,l), y \in (-h,h)\}$ subject to strong (that is point-wise prescribed) traction boundary conditions on the horizontal surfaces,

$$\sigma_{xy}(x, y = h) = f_x^1(x), \quad \sigma_{yy}(x, y = h) = f_y^1(x)$$
$$\sigma_{xy}(x, y = -h) = f_x^2(x), \quad \sigma_{yy}(x, y = -h) = f_y^2(x) \tag{27}$$

and weak (that is resultant prescribed) boundary conditions on the vertical surfaces,

$$\int_{-h}^{h}\sigma_{xy}(x=l,y)dy = Q_2, \quad \int_{-h}^{h}\sigma_{xy}(x=-l,y)dy = Q_1$$
$$\int_{-h}^{h}\sigma_{xx}(x=l,y)dy = N_2, \quad \int_{-h}^{h}\sigma_{xx}(x=-l,y)dy = N_1 \tag{28}$$
$$\int_{-h}^{h}y\sigma_{xx}(x=l,y)dy = M_2, \quad \int_{-h}^{h}y\sigma_{xx}(x=-l,y)dy = M_1$$

where $(N_1, Q_1, M_1, N_2, Q_2, M_2)$ are the prescribed axial force, shear force and bending moment per unit depth of the cross section, respectively. The loadings$(f_y^1, f_y^2, f_x^1, f_x^2)$, representing normal and shear traction components on the horizontal surfaces, are as-sumed to be square integreble[6] and consistent with global equilib-rium of the sublayer, but otherwise arbitrary. Note that the superscript on the traction components (f_x^i, f_y^i) indicates top ($i = 1$) or bottom ($i = 2$) surface (for resultants (N_i, Q_i, M_i) the subscript indicates left ($i = 1$) or right ($i = 2$) surface). Depending upon whether the sublayer surface is interior or exterior the func-tions $(f_x^1, f_y^1, f_x^2, f_y^2)$ are regarded as applied boundary tractions or, reactive displacement jump dependent interface tractions. The equations of global equilibrium representing force and moment balance are given by,

$$N_2 - N_1 + \int_{-l}^{l}[f_x^1(x) - f_x^2(x)]dx = 0, Q_2 - Q_1 + \int_{-l}^{l}[f_y^1(x) - f_y^2(x)]dx = 0$$
$$l(Q_2 + Q_1) + (M_1 - M_2) + \int_{-l}^{l}x[f_y^1(x) - f_y^2(x)]dx - h\int_{-l}^{l}[f_x^1(x) + f_x^2(x)]dx = 0 \tag{29}$$

where use has been made of the weak boundary conditions (28).

In the Appendix stress function solutions that satisfy the stress function equation (5) and the global equilibrium/boundary condi-tions are constructed in the form of an eigenfunction expansion. By writing normal and shear loads $(f_x^1, f_y^1, f_x^2, f_y^2)$ on the upper and lower surfaces as mean convergent Fourier expansions a concise form for the stress and displacement fields within a single sublayer can be obtained. Of particular importance to the development of interfacial integral equations for the sublayer system are the boundary displacement components $u_x(x, y = \pm h)$, $u_y(x, y = \pm h)$ and these are given by (A.4).

Integral equations governing the separation/slip of a defect evolving along a straight predetermined cohesive interface can be obtained by employing (A.4) for two materially identical sublay-ers and properly identifying applied boundary loads and reactive, displacement jump dependent cohesive tractions (Fig. 8). An addi-tional sub or superscript is now included which indicates sublayer number (for example the j subscript in $(f_x^{ij}, f_y^{ij}, N_{ij}, Q_{ij}, M_{ij})$). Thus, if the single sublayer solution is applied to the upper (lower) sublay-er then f_x^{11}, f_y^{11} (f_x^{22}, f_y^{22}) represents applied boundary loads while $f_x^{21} = f_x^{12}$, $f_y^{21} = f_y^{12}$ are cohesive traction-separation/slip relations which may be written as $f_x^{21}(x, u(x), v(x)), f_y^{21}(x, u(x), v(x))$. The nor-malized displacement jump components $u(x), v(x)$ are defined by $u = [\mathbf{u}] \bullet \mathbf{e}_x/l$, $v = [\mathbf{u}] \bullet \mathbf{e}_y/l$ where the displacement jump vector $[\mathbf{u}]$ is the difference $\mathbf{u}(x, y_1 = -h_1) - \mathbf{u}(x, y_2 = h_2)$, $\mathbf{u}(x, y_1 = -h_1)$ ta-ken in the top sublayer and $\mathbf{u}(x, y_2 = h_2)$ taken in the bottom sub-layer. Integral equations governing the normal component of displacement jump (or separation) v and tangential component (or shear slip) u can be obtained by writing (A.4) for the lower (upper) surface of the top (bottom) sublayer and subtracting. This leads to,

---

[6] A function which is piecewise continuous with a finite number of bounded jump discontinuities.
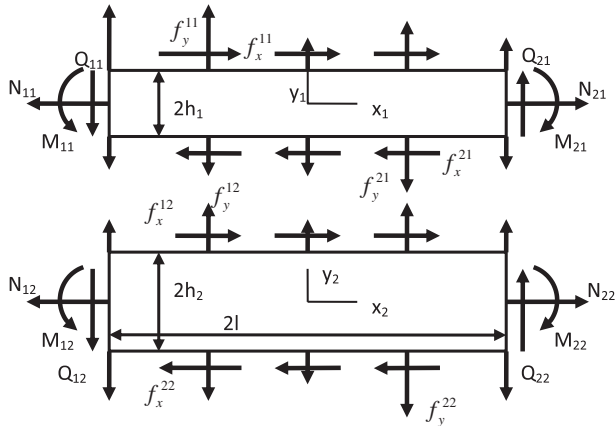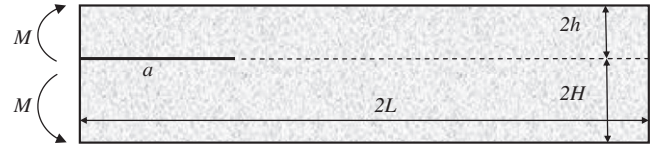
Fig. 8. Two sub layer system.

Fig. 9. The edge defect layer under end moments. $\eta = h/H$.

normalized by half-length l. (For explicit expressions of these quantities as well as the kernel functions see the Appendix.) The rigid body equilibrium terms u_R, v_R, ω_1 appearing in the integral equations are handled in the following way. If an equilibrium set of applied boundary loads are chosen for the entire sublayer system then satisfaction of equilibrium equations (29) for one sublayer implies satisfaction of equilibrium for the second sublayer. Thus we have available three additional equations (29) to solve for three of the 6 rigid body displacement quantities associated with the two individual sublayers. In (30) we have fixed the bottom sublayer against rigid translation and rotation. The remaining 3 rigid body terms associated with the top sublayer will be obtained using (29). A prescription of the quantities f_x^{21}, f_y^{21} as functions of interface coordinate x and normal separation v and shear slip u completes the governing equations to the problem. The system (30) and (29) is therefore well posed and its solution $u(x)$, $v(x)$ enables the determination of traction distributions $f_x^{21}(x), f_y^{21}(x)$ along the defect line. If desired, the stress field within the sublayers can now be determined since all the boundary conditions are available explicitly.

The solution to system (30) and (29) are obtained by expanding the separation/slip fields $u(x)$, $v(x)$ in eigenfunctions of the kernels. The substitution of these expansions reduces the system to an infinite set of nonlinear algebraic equations which are then truncated and solved for the unknown mode multipliers. A computer program, expressly written for this purpose, solves the equations numerically using the Newton-Raphson method with integrals explicitly appearing in the algebraic equations evaluated using a composite Simpson formula. The results appearing below are based on a 256 mode truncation of the governing equations. This approximation was chosen because it represents a good balance between (i) solution smoothness, (ii) solution precision and (iii) available computer power. Solution precision was tested with different numbers of modes to ensure that truncation errors were insignificant in the sense that errors did not affect (i) the qualitative features of the cohesive separation/slip behavior or (ii) the stress distributions.

$$u(x) = u_R + \omega_1 \gamma_1 + h_x^R(x) + \int_{-l}^{l} K_{xy}^{11}(x,x') f_y^{11}(x') dx'$$
$$+ \int_{-l}^{l} K_{xx}^{11}(x,x') f_x^{11}(x') dx' + \int_{-l}^{l} K_{xy}^{22}(x,x') f_y^{22}(x') dx'$$
$$+ \int_{-l}^{l} K_{xx}^{22}(x,x') f_x^{22}(x') dx' + \int_{-l}^{l} K_{xy}(x,x') f_y^{21}(x', u(x'), v(x')) dx'$$
$$+ \int_{-l}^{l} K_{xx}(x,x') f_x^{21}(x', u(x'), v(x')) dx'$$

$$v(x) = v_R - \omega_1 x + h_y^R(x) + \int_{-l}^{l} K_y^{11}(x,x') f_y^{11}(x') dx'$$
$$+ \int_{-l}^{l} K_{yx}^{11}(x,x') f_x^{11}(x') dx' + \int_{-l}^{l} K_{yy}^{22}(x,x') f_y^{22}(x') dx'$$
$$+ \int_{-l}^{l} K_{yx}^{22}(x,x') f_x^{22}(x') dx' + \int_{-l}^{l} K_{yx}(x,x') f_x^{21}(x', u(x'), v(x')) dx'$$
$$+ \int_{-l}^{l} K_{yy}(x,x') f_y^{21}(x', u(x'), v(x')) dx' \tag{30}$$

where $K_{xx} = K_{xx}^{21} - K_{xx}^{12}$, $K_{xy} = K_{xy}^{21} - K_{xy}^{12}$, $K_{yx} = K_{yx}^{21} - K_{yx}^{12}$, $K_{yy} = K_{yy}^{21} - K_{yy}^{12}$ and γ_1 is the thickness ratio of the first layer (i.e., h_1/l). Note that the first four integrals in each integral equation represents the effect on behavior arising from the pointwise prescribed boundary loads on the upper and lower surfaces. The functions h_x^R and h_y^R are simply the differences between h_x^1, h_x^2 and h_y^1, h_y^2 respectively,
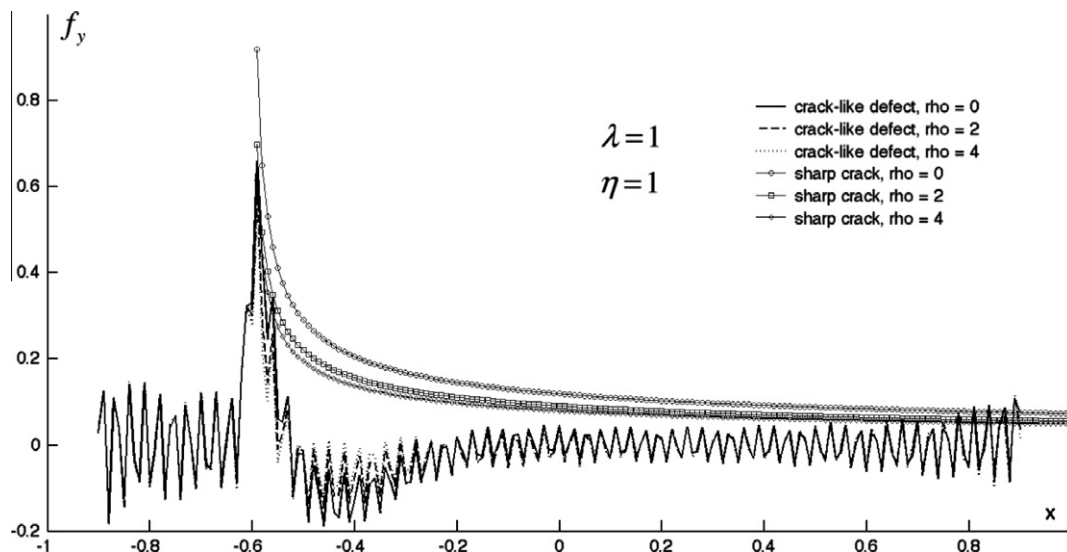

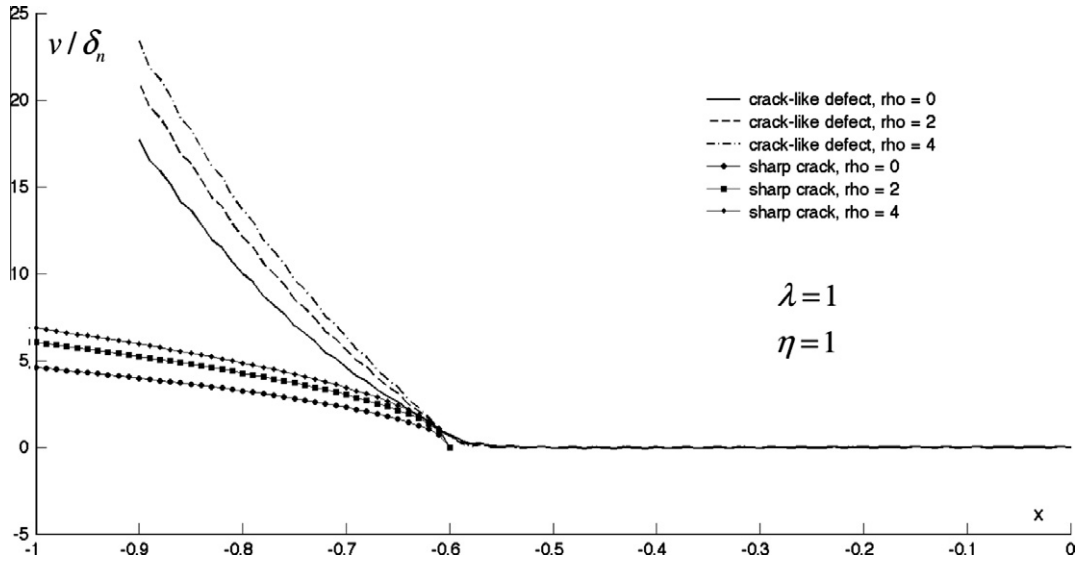**Fig. 10a.** Distribution of normal traction along defect line. Cubic.

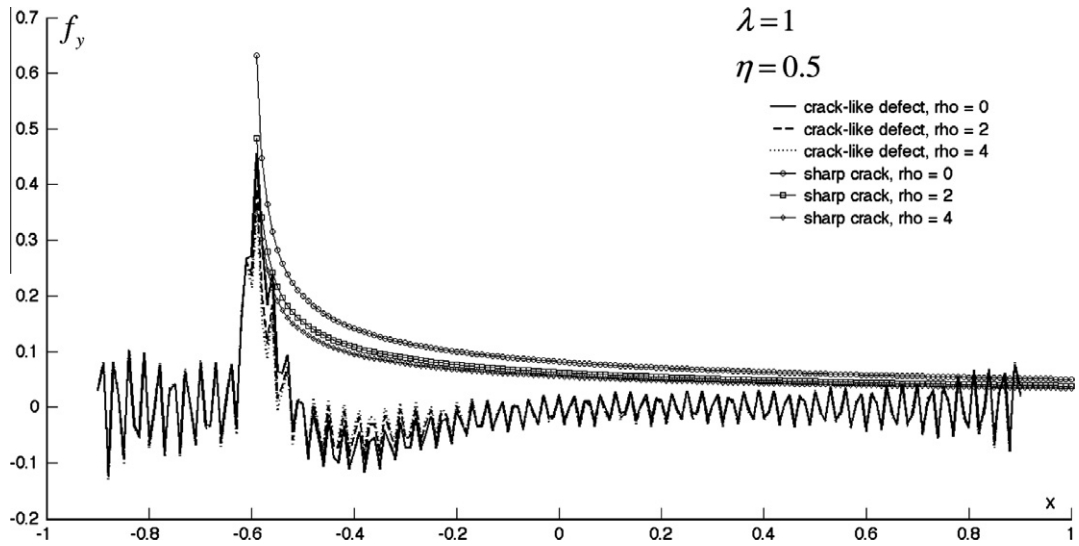**Fig. 10b.** Distribution of normal cohesive separation along defect line. Cubic.

Fig. 11a. Distribution of normal traction along defect line. Cubic.
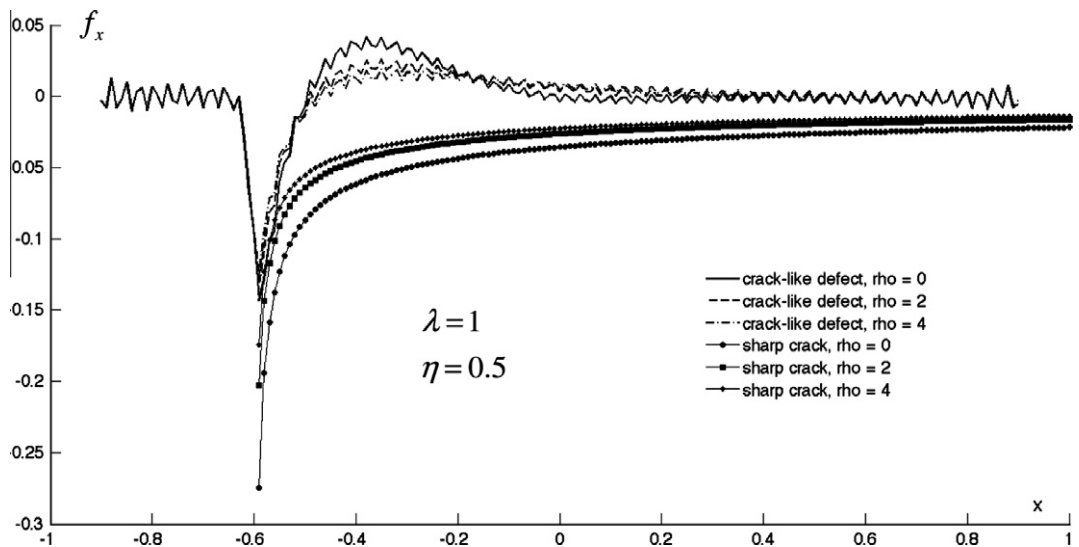

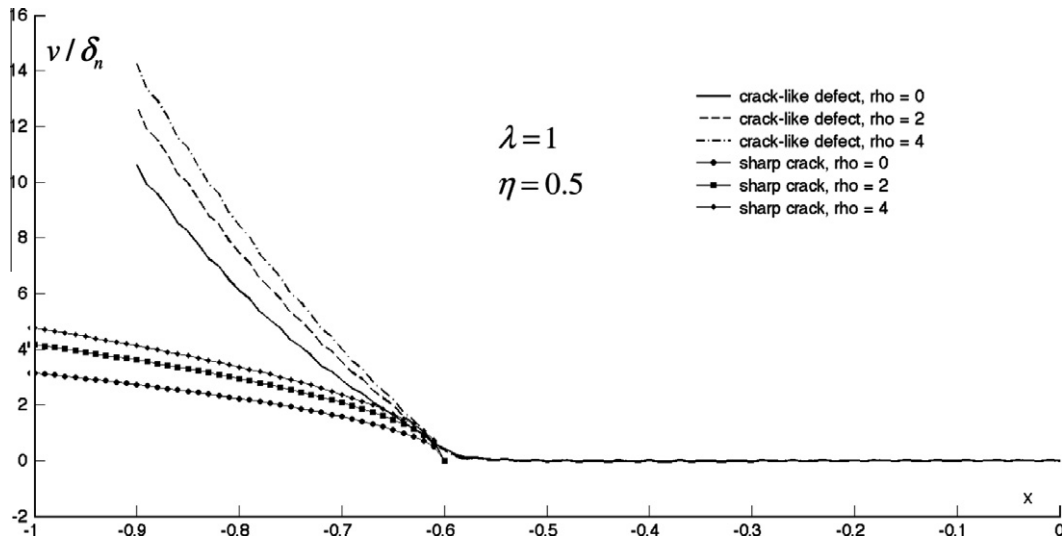**Fig. 11b.** Distribution of shear traction along defect line. Cubic.

Fig. 12a. Distribution of normal cohesive separation along defect line. Cubic.
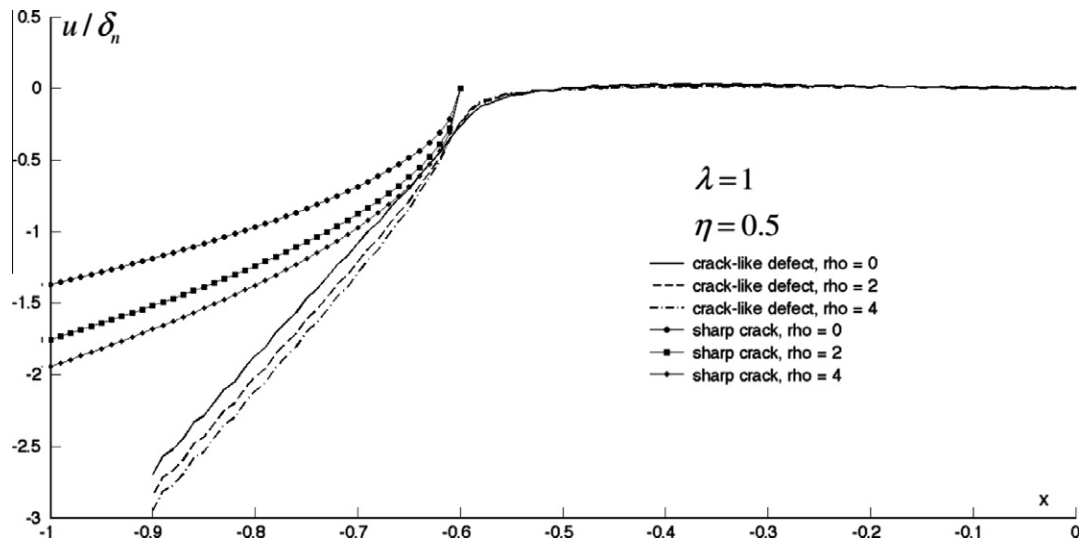

Fig. 12b. Distribution of shear cohesive slip along defect line. Cubic.

3.2. The edge notched layer subject to end moments. ρ dependence

The solution to the problem of an edge notched layer, separated along a straight cohesive interface by end moments (Fig. 9), is now considered for cubic materials and, for fully orthotropic materials via rescaling. In the former case we utilize the computational procedure described above while in the later case rescaling the solution for materials with cubic symmetry yields the desired results. Of particular interest is the effect of shear parameter ρ on behavior. Note that the parameter $\eta = h/H$ characterizes departures from geometric symmetry, i.e., departures from $\eta = 1$, where, at this value of η, there is no shear traction or shear slip on the cohesive interface. Also, further note that the moment M (per unit depth) has been normalized by $L^2 \sigma_{max}$.

In Figs. 10–14 we will consider the *cohesive defect* approximation to *static sharp crack* behavior and then relax this approximation, thereby allowing for defect evolution, in the figures that follow. Note that in these figures the moment is taken to be $M = 0.005$. Fig. 10 contains distribution plots of normalized (with respect to the interface strength σ_{max}) normal traction (Fig. 10a),

and normalized normal separation (Fig. 10b), along the crack line for various values of shear parameter ρ for material with cubic symmetry. For comparison purposes the sharp crack solution (Suo, 1990) is also plotted at those values of ρ. The *sharp crack* and the *cohesive defect* solutions for the normal traction (Fig. 10a) generally show the same trend at the crack tip but differ markedly ahead of it. The compressive region in front of the tip is captured by the cohesive defect solution but completely missed by the asymptotic singular solution of Suo (1990). Companion curves of normalized normal separation are shown in Fig. 10b. The sharp crack asymptote cannot capture the opening behind and away from the tip although both solutions yield correct behavior in front of the tip, i.e., vanishing normal separation. Note that in the cohesive interface calculation, interface compression is effectively resisted by the very stiff compressive tail of the exponential force law in normal mode (Fig. 2). As expected, both Figs. 10a and 10b indicate that the effect of shear parameter ρ is relatively weak for this geometrical and loading configuration. Furthermore, note that graphs of separation (Fig. 10b), which are obtained directly in the present formulation, reveal very small oscillations using
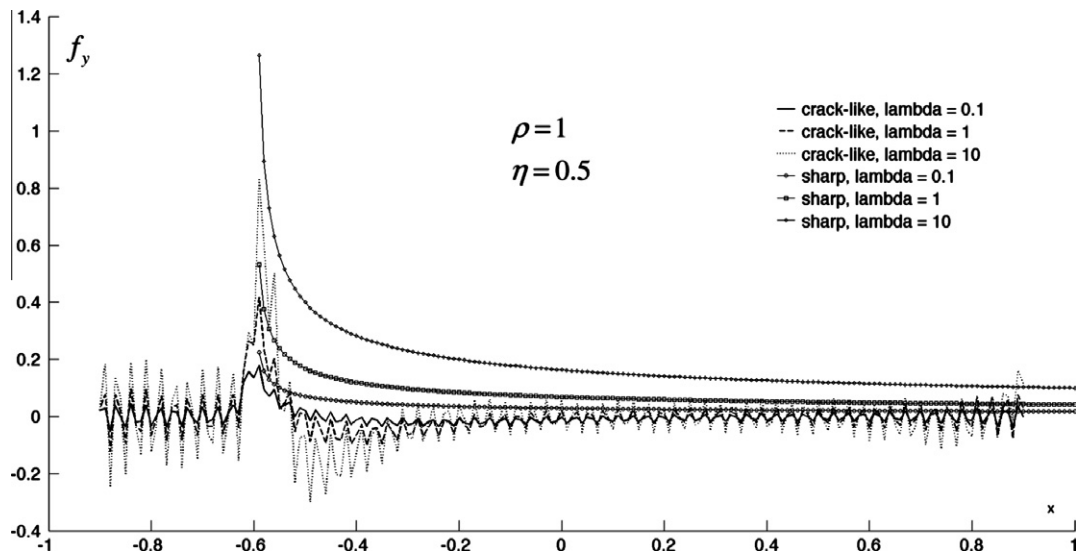
Fig. 13a. Distribution of normal traction along defect line. Degenerate orthotropic.
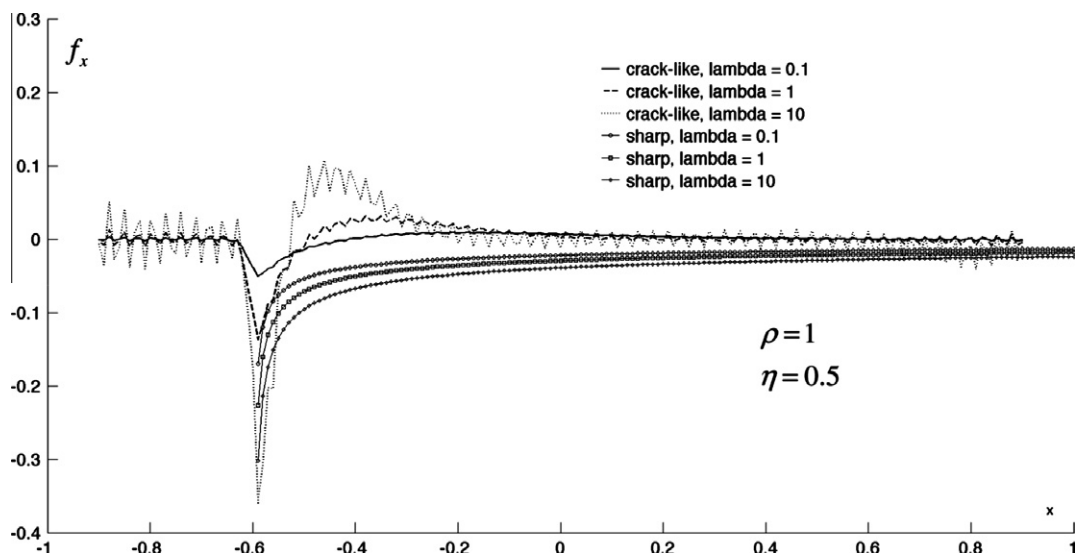

Fig. 13b. Distribution of normal traction along defect line. Degenerate orthotropic.

256 modes. Larger oscillations in interface traction components (Fig. 10a) occur because of the amplification effect of the force law. Large derivatives on either side of the maxima of the normal and shear interface traction components work to amplify minor oscillations that exist in the displacement jump components. Removing these oscillations by smoothing out the displacement jump components was not carried out because our interest is in the qualitative aspects of the global distributions and not the specific values of interface traction components at a point. Figs. 11 and 12 are plots of the same behavior except for the case where the symmetry parameter is $\eta = 0.5$. The normal traction/separation behavior (Figs. 11a and 12a) is very similar to that of $\eta = 1$ (Fig. 10) in that there is a weak dependence of shear parameter ρ and the same basic features of the curves are maintained. The magnitude of the edge displacement is smaller in the $\eta = 0.5$ case and this reflects a transition to *peel* type behavior. In contrast to the symmetric case of Fig. 10, here the geometric asymmetry induces a shear traction (Fig. 11b) and a shear slip (12b). As expected for this geometry, f_x is of smaller magnitude then f_y. Furthermore,

Fig. 11b clearly shows a region of shear traction reversal which must occur in order to satisfy global equilibrium of a single layer.

The insensitivity of behavior to ρ in the edge notched layer configuration allows one to predict fully orthotropic behavior from degenerate orthotropic ($\rho = 1$) response. Figs. 13 and 14 depict response for asymmetrical ($\eta = 0.5$) geometry and for a range of values of stiffness ratio λ. In particular, Fig. 13 contains graphs of normal (Fig. 13a) and shear (Fig. 13b) cohesive traction while Fig. 14 contains graphs of normal cohesive separation (Fig. 14a) and cohesive shear slip (Fig. 14b). Also depicted is the sharp crack solution. Note that as in previous figures there is a compressive region (Fig. 13a) and a shear traction reversal (Fig. 13b) ahead of the crack tip. Furthermore, the separation v/δ_n increases with stiffness parameter λ. This is to be expected based on the static sharp crack results of Suo (1990) and, because an increased λ indicates a decreased bending stiffness (i.e., a smaller E_1). One of the strengths of the cohesive interface approach is that it naturally allows for defect propagation under load. For the edge notched layer configuration we now relax the sharp crack approximation by requiring the
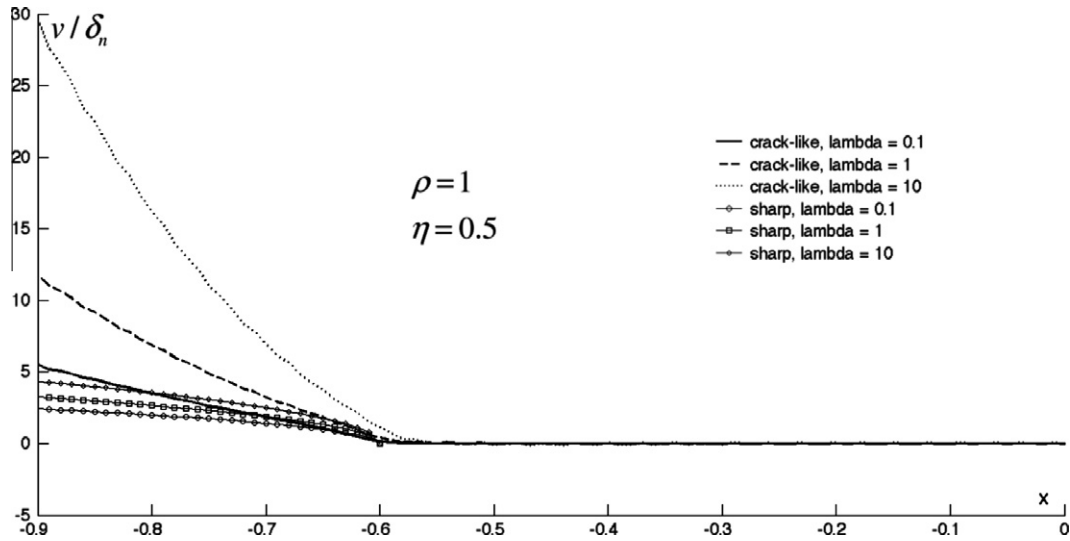
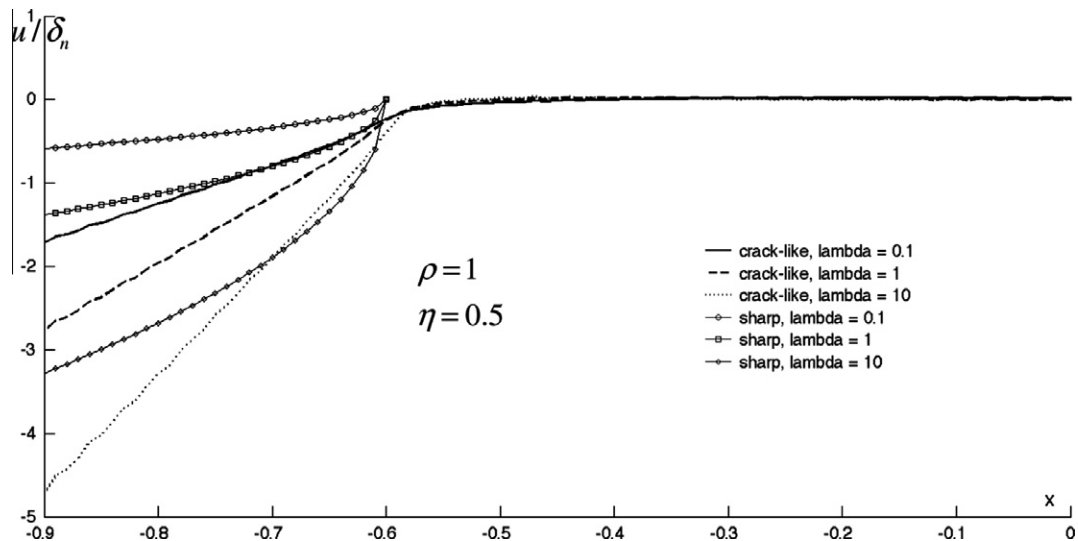**Fig. 14a.** Distribution of normal cohesive separation along defect line. Degenerate orthotropic.

Fig. 14b. Distribution of shear cohesive slip along defect line. Degenerate orthotropic.

applied moment to range over values large enough to precipitate significant defect growth. The basic mechanics of cohesive defect propagation in layered systems was described in Nguyen and Levy (2009). There, the problem of an isotropic bilayer with an edge defect subject to applied shear forces was analyzed. In that work two modes of defect propagation were identified, both of which ultimately result in an unzipping of the interface characterized by an unbounded rate $d\hat{a}/dP$ attained at the *unzip load*, i.e., the maximum value of load (shear force P) required to sustain equilibrium. Here, $\hat{a}(P)$ is the evolving defect length (with $\hat{a}(P = 0) = a$) defined by onset criteria for separation or slip, i.e., the defect tip is located at the point which first satisfies $u(x, P) = \delta_t$ or $v(x, P) = \delta_n$. *Brittle defect growth* is distinguished by a rate of increase of defect length with load which becomes large at small values of load P and length $\hat{a}(P)$ while *ductile defect growth* is characterized by a rate which becomes large at large values of load P and length $\hat{a}(P)$. Thus, the qualitative difference in response for *ductile behavior* and for *brittle behavior* is that in the ductile case, the interface defect opens up and extends gradually with application of load. Brittle behavior

has the defect behaving in an almost stationary manner, opening a small amount but without appreciable extension until a critical P precipitates an abrupt unzipping behavior. In Nguyen and Levy (2009) the parameter which controls this behavior is the *interface force length* δ_n. Here we are concerned with a similar edge defect geometry albeit with a slightly different loading (applied moments not shear forces) and a uniform orthotropic layer (and not an isotropic bilayer). In what follows we will address the question: *at a fixed δ_n, can a change in stiffness ratio λ precipitate a transition from ductile to brittle interface response?* Note that in all remaining calculations, unless otherwise noted, the following parameter values are assumed: $\rho = 2$, $\eta = 0.5$, $E = 1000\sigma_{max}$, $v = 0.25$, $\delta_n = 0.01$, $\gamma_1 = 0.1$, $a = 0.5$ (other parameter values required will be introduced in the text that follows or, when they appear directly in the figures).

Figs. 15a and 15b contain plots of normal separation distribution and shear slip distribution along the defect line for a stiffness ratio $\lambda = 0.1$. At this parameter value the figures indicate a gradual, ductile evolution with load of normal separation and shear slip. Here, the defect unzips the interface at a maximum value of load,
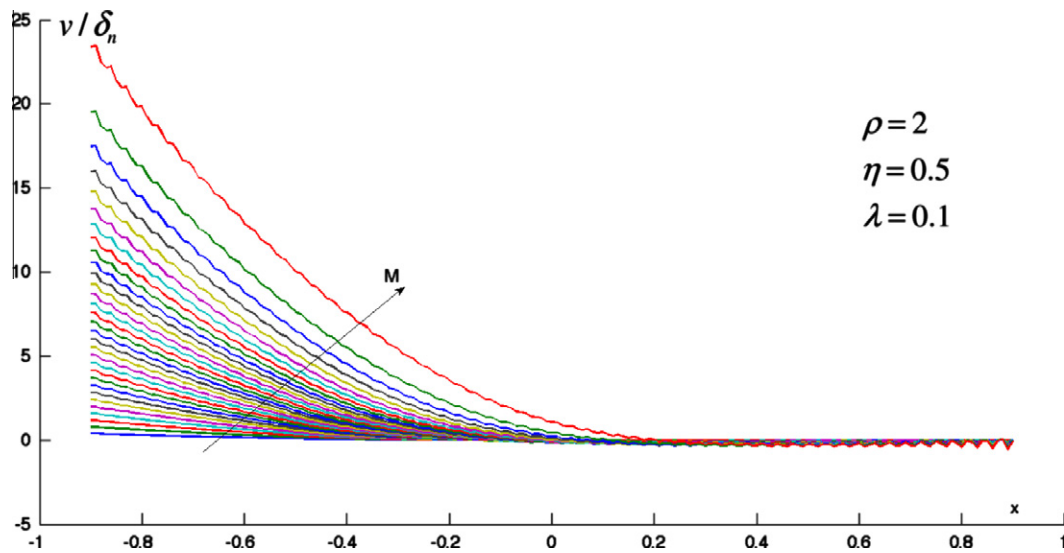
Fig. 15a. Separation distribution along defect line. Load step 0.01. Unzip load $M_u = 0.31$.
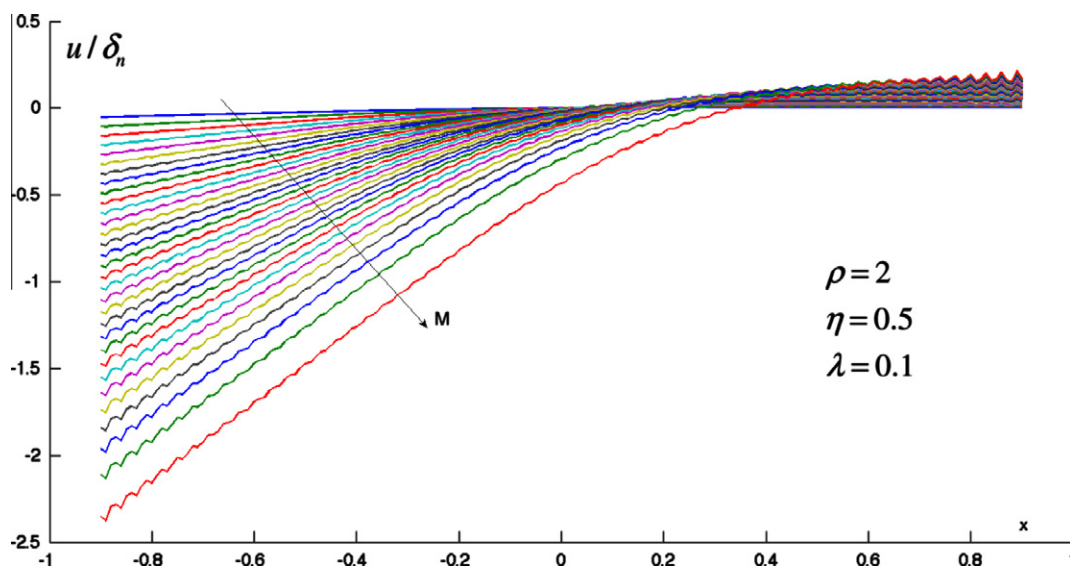

Fig. 15b. Shear slip distribution along defect line. Load step 0.01. Unzip load $M_u = 0.31$.

$M_u = 0.31$. Figs. 16a and 16b are similar to 15a and 15b except that the stiffness ratio has been increased 100-fold to $\lambda = 10$. The resulting noticeably different behavior is remarkable in that there is now a critical *jump load* $M^* = 0.095$ which precipitates an abrupt or brittle opening with a coincident extension of the defect. Following this transition there is a loading region where the defect continues to evolve prior to unzip at a load of $M_u = 0.175$. Furthermore, note that the maximum magnitude of the normal separation at unzip is nearly an order of magnitude larger for the brittle process (i.e., when $\lambda = 10$). This can be expected owing to the fact that, for this value of λ, $E_1 < E_2$ and the primary deformation mechanism appears to be bending. Both Figs. 15 and 16 indicate very small negative values of v/δ_n for intervals ahead of the evolving defect tip. This kind of interpenetration indicates a contact zone because the interface force law in normal mode actively resists material interpenetration through a very high compressive stiffness (see Fig. 2). Note as well that the shear slip for both stiffness ratios is an order of magnitude smaller than the normal separation. This is not surprising as the load and defect geometries indicate a primarily

normal mode process. Figs. 17a and 17b are plots of normal and shear traction along the defect line for a stiffness ratio $\lambda = 0.1$. These graphs are consistent with the separation and shear slip distributions of Figs. 15a and 15b. As expected the magnitude of the shear traction f_x is an order of magnitude less than the normal traction f_y. Furthermore, the plots clearly show regions of interface compression and shear traction reversal which must occur in order to satisfy global equilibrium of a single sub layer. Fig. 18 is a plot of the evolving defect length $\hat{a}$ versus load M for two groups of curves: the $\eta = h/H = 1$ group,[7] and the $\eta = h/H = 0.5$ group, both of which contain three curves representing the response under stiffness ratios $\lambda = 0.1, 1, 10$. All curves begin at the initiation load and terminate at the unzip load M_u, i.e., the maximum load attainable prior to the breakdown of equilibrium coincident with a large (theoretically unbounded) growth rate $d\hat{a}/dM$. The figure indicates that for both groups, small values of stiffness ratio supports ductile defect growth

---

[7] Recall that values of η different from unity characterize departures from symmetry.
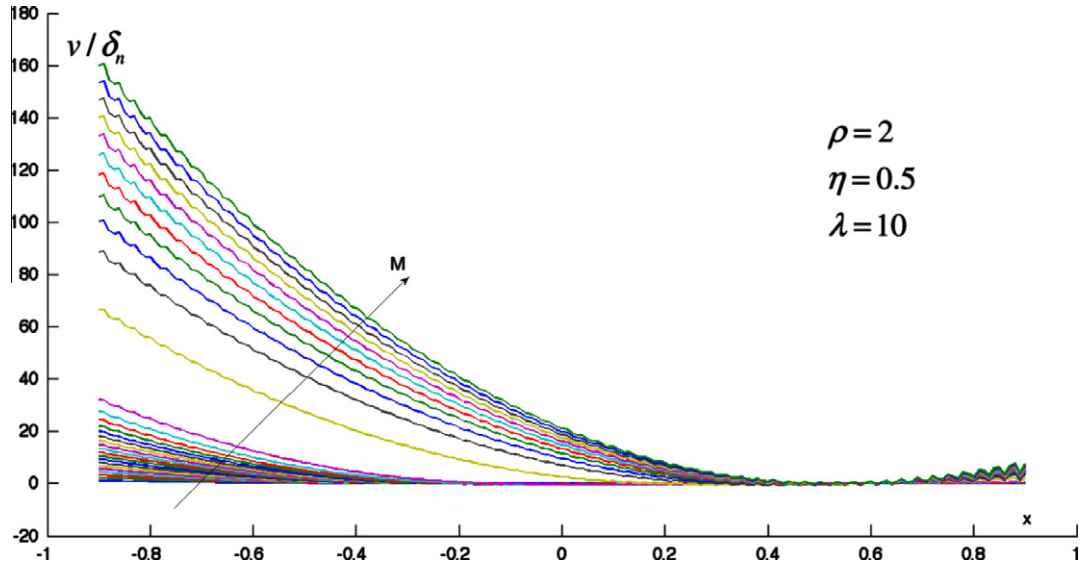
Fig. 16a. Separation distribution along defect line. Load step 0.005. Unzip load M_u = 0.175. Jump load M^* = 0.095.
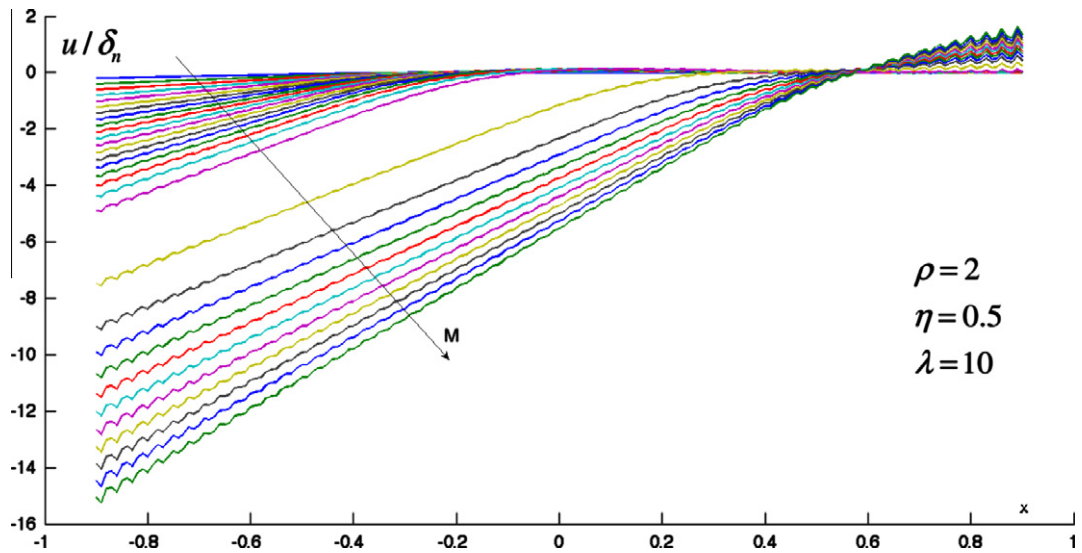

Fig. 16b. Shear slip distribution along defect line. Load step 0.005. Unzip load M_u = 0.175. Jump load M^* = 0.095.
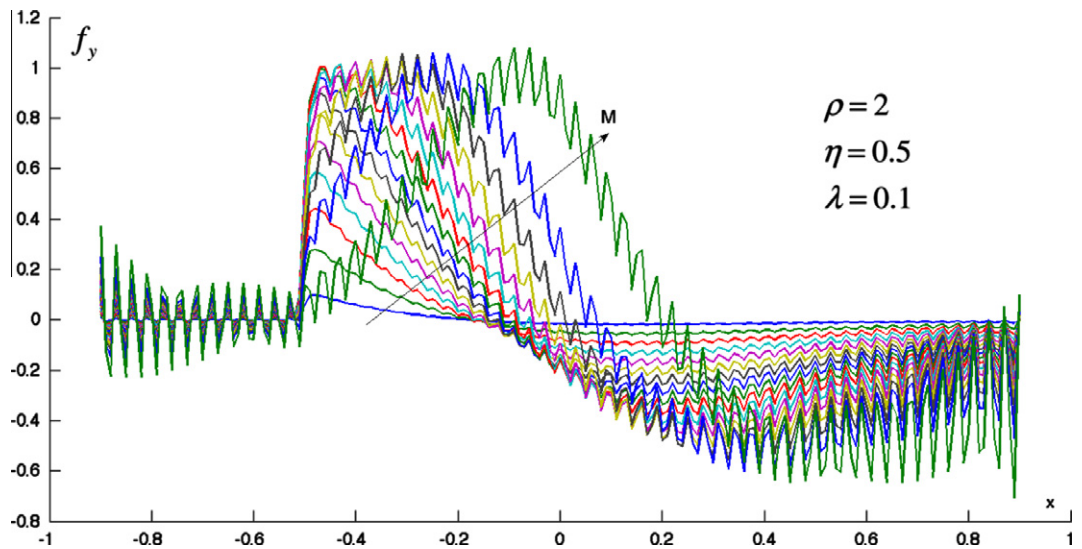

Fig. 17a. Normal traction distribution along defect line. Load step 0.02. Unzip load M_u = 0.31.
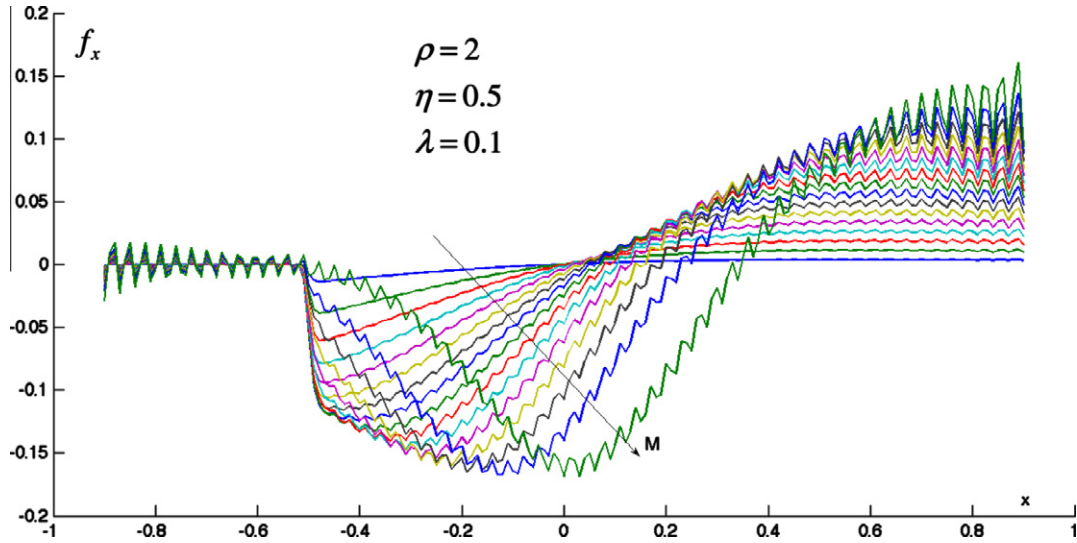
Fig. 17b. Shear traction distribution along defect line. Load step 0.02. Unzip load M_u = 0.31.
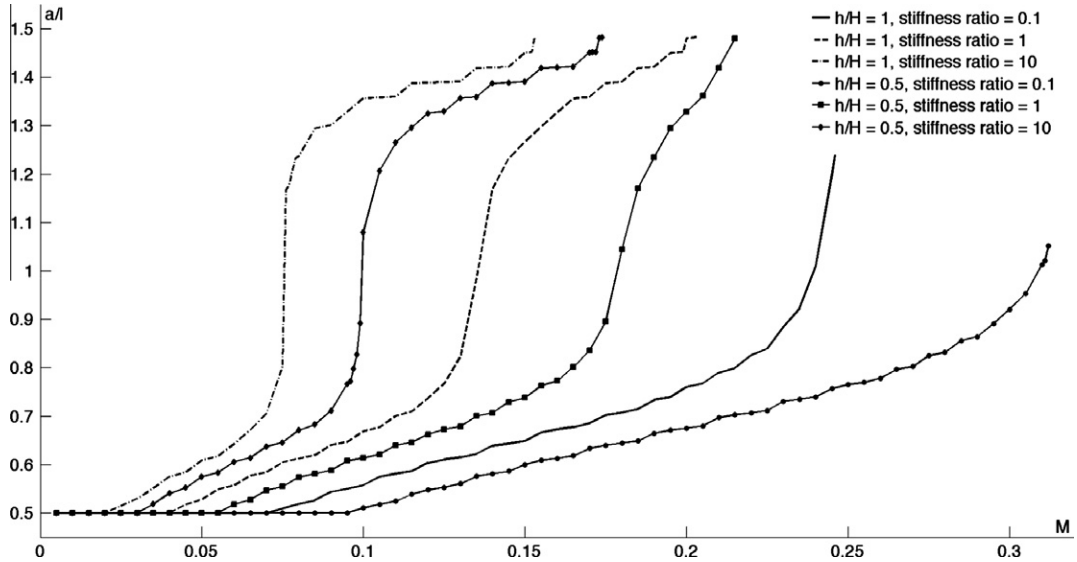

Fig. 18. Defect length versus load. M_u for curves (from left) (0.155, 0.175, 0.21, 0.22, 0.25, 0.315).

(e.g., $(\eta, \lambda) = (1, 0.1), (0.5, 0.1)$) characterized by a relatively large, smooth increase of $\hat{a}$ with M terminating at an unzip load M_u. In contrast consider the curves obtained by increasing the stiffness ratio λ 10-fold to $(\eta, \lambda) = (1, 1), (0.5, 1)$ and then 100-fold to $(\eta, \lambda) = (1, 10), (0.5, 10)$. The curves undergo a transition from continuous defect growth to what appears to be a jump discontinuity in defect length at a critical value of load (*jump load*) M^*. For stiffness ratio λ=10, this is indicated by a vertical line which is really just a measure of the magnitude of the jump discontinuity and is a manifestation of the load control algorithm used in the analysis. We expect that displacement control would yield unstable solutions as well which would probably give rise to an "S" shaped extension-load curve.

In any event the load M^* does not lead to unzipping of the interface and there exists an interval of load beyond M^*, i.e., $M \in (M^*, M_u)$ which results in an increase of defect length $\hat{a}$ with M, although at a diminishing rate. Ultimately this process terminates

at the unzip load M_u at an unbounded growth rate $d\hat{a}/dM$. Note that the unzip load M_u for more or less ductile defect evolution at stiffness ratio $\lambda = 0.1$ is greater than the jump load M^* and the unzip load M_u for $\lambda = 10$ but, the associated defect lengths $\hat{a}$ are such that for $\lambda = 0.1$ $\hat{a}$ at unzip is greater than $\hat{a}$ at jump, but less than $\hat{a}$ at unzip, for $\lambda = 10$. For this reason an elevated stiffness ratio leads to a kind of quasi-brittle defect growth response. Finally, note that decreasing $\eta = h/H$ from unity (i.e., departures from symmetry (Fig. 9)) effectively elevates the load required for a given defect length. This is indicated by Fig. 18 for all values of stiffness ratio λ.

4. Conclusions

In this paper we have demonstrated that orthotropy rescaling of the nonlinear *cohesive defect* problem preserves some of the

key features of the rescaling of linear *static sharp crack* problems. In particular, we have shown that solutions to degenerate orthotropic problems ($\rho = 1$) can be obtained from isotropic solutions while solutions to fully orthotropic problems ($\rho \neq 1$) can be obtained from cubic symmetry solutions. In the former situation we have utilized existing solutions to two distinct isotropic problems (symmetrical opening of a cohesive defect in a layer; stability of interfacial separation in a trilayer system) to obtain degenerate orthotropic response. In the later case we have presented an exact, integral equation formulation of nonlinear cohesive growth in a layer composed of cubically symmetric material and then rescaled to obtain fully orthotropic solutions. The utility of this methodology, for the cubically symmetric problem, remains the same as for the isotropic problem, i.e., as stated in Nguyen and Levy (2011): the efficacy of this approach is that (i) it lacks the conceptual limitations of Euler–Bernoulli beam theory, (ii) it enables the determination of interface separation/slip behavior without solving for the detailed elastic fields within the layers and (iii) it approaches the generality of finite element analysis (FEA) for the class of systems considered, i.e., linear elastic layers.

For the problem of defect growth in the cubically symmetric, edge notch bend configuration detailed results have been obtained and key features of the response elucidated. In particular, in this configuration we have demonstrated that the solution has a weak dependence on shear parameter ρ enabling solutions to be estimated from isotropic ones. This is a well known attribute of many solutions to orthotropic static, sharp crack problems. Furthermore, it was shown that under increasing orthotropic stiffness ratio a transition occurs from a ductile (gradual, smooth) defect evolution to a quasi-brittle type of behavior characterized by a discontinuous jump in (i) defect extension and (ii) normal separation and shear slip. Beyond the jump load that precipitates this behavior there is additional smooth defect extension (although at a lower rate) prior to unzipping of the interface. Note that this behavior contrasts with truly brittle response that occurs, for example, when an isotropic bilayer containing an edge defect is pulled apart by equal and opposite shear forces (Nguyen and Levy, 2009). In that problem reducing the interface energy signals a transition from smooth ductile defect growth, characterized by unbounded defect growth rates at large defect lengths and large unzip loads, to brittle defect growth characterized by unbounded defect growth rates at small defect lengths and small unzip loads. In the latter case the discontinuous transition in growth rate occurs at the unzip load and, in contrast to the problem considered here, there is no stable defect growth beyond this load.

Furthermore, while this paper treats the problem of defect evolution in a homogeneous orthotropic layer a natural extension is to consider defect growth along an interface(s) in a heterogeneous, orthotropic multilayer composite. Recall that for the homogeneous layer the device utilized was a predetermined cohesive interface, along which a defect will evolve, which separates the layer into the two materially uniform sub layers. In the multilayer composite problem individual layers will have different (orthotropic) material properties so that each layer will require distinct rescaling characteristics. The nonlinear coupling of any two layers across a cohesive interface gives rise to ambiguity in the definition of interface displacement jump. This is an important difference between defect evolution within a single homogeneous layer and at an interface in a multilayer composite. Future work will address this issue and provide an analysis of interfacial defect evolution in the orthotropic multilayer composite.

Appendix A

Stress function solutions that satisfy the stress function equation (5) may be expressed in the form of an eigenfunction expansion,

$$\varphi = \sum_{n=0}^{\infty} \psi_n(y) \cos \alpha_n x + \sum_{n=1}^{\infty} \eta_n(y) \sin \alpha_n x, \quad \alpha_n = \frac{n\pi}{l} \tag{A.1}$$

with ψ_n, η_n given by,

$$\psi_0(y) = C_0 xy + C_1 x^2 + C_{30} y^2 + C_{40} y^3 + C_2 x^2 y + C_3 xy^2 + C_4 xy^3$$

$\underline{\rho < 1}$

$$\psi_n(y) = C_{1n} \cosh \alpha_n \gamma y \cos \alpha_n \zeta y + C_{2n} \sinh \alpha_n \gamma y \cos \alpha_n \zeta y$$
$$+ C_{3n} \cosh \alpha_n \gamma y \sin \alpha_n \zeta y + C_{4n} \sinh \alpha_n y \sin \alpha_n \zeta y$$

$$\eta_n(y) = D_{1n} \cosh \alpha_n \gamma y \cos \alpha_n \zeta y + D_{2n} \sinh \alpha_n \gamma y \cos \alpha_n \zeta y$$
$$+ D_{3n} \cosh \alpha_n \gamma y \sin \alpha_n \zeta y + D_{4n} \sinh \alpha_n y \sin \alpha_n \zeta y, \quad n = 1, 2, 3, \ldots$$

$\underline{\rho > 1}$

$$\psi_n(y) = C_{1n} \cosh \alpha_n \gamma y \cosh \alpha_n \zeta' y + C_{2n} \sinh \alpha_n \gamma y \cosh \alpha_n \zeta' y + C_{3n}$$
$$\times \cosh \alpha_n \gamma y \sinh \alpha_n \zeta' y + C_{4n} \sinh \alpha_n \gamma y \sinh \alpha_n \zeta' y$$

$$\eta_n(y) = D_{1n} \cosh \alpha_n \gamma y \cosh \alpha_n \zeta' y + D_{2n} \sinh \alpha_n \gamma y \cosh \alpha_n \zeta' y$$
$$+ D_{3n} \cosh \alpha_n \gamma y \sinh \alpha_n \zeta' y + D_{4n} \sinh \alpha_n \gamma y \sinh \alpha_n \zeta' y,$$
$$n = 1, 2, 3, \ldots$$

where $\gamma = \sqrt{\frac{1+\rho}{2}}$, $\zeta = \sqrt{\frac{1-\rho}{2}}$, $\zeta' = -\sqrt{\frac{\rho-1}{2}}$. Note the isotropic case ($\rho = 1$) has been treated in Nguyen and Levy (2009, 2011) and will not be considered further (although it can be obtained from (A.2) by appropriate handling of the degenerate terms). The structure of the function ψ_0 involves non-Fourier terms for the stress function (xy, x^2) which are included because they give rise to Fourier terms for the stresses. Additional terms ($x^2 y, xy^2, xy^3$) capture axial variation of shear force, normal force and bending moment required by the weak boundary conditions on the surfaces at $x = \pm l$. The 7 constants $\{C_0, C_1, C_2, C_3, C_4, C_{30}, C_{40}\}$ together with the 8 sets of coefficients are determined by the 4 strong boundary conditions (27) on $y = \pm h$ plus the 3 weak conditions on the left $x = -l$ end of the sublayer (28)$_{2,4,6}$. (Note that the 4 strong boundary conditions represent 12 conditions on the constants or sets of coefficients.) The 3 additional weak boundary conditions on $x = l$ (28)$_{1,3,5}$ are used to obtain the resultant normal, shear and moment at the right end of the sublayer. It is not hard to show that satisfaction of all of these conditions implies satisfaction of global equilibrium (29).

If the normal and shear loads ($f_x^1, f_y^1, f_x^2, f_y^2$) on the upper and lower surfaces are written as mean convergent Fourier expansions, e.g.,

$$f_y^1(x) = \sum_{n=0}^{\infty} f_{yen}^1 \cos \alpha_n x + \sum_{n=1}^{\infty} f_{yon}^1 \sin \alpha_n x$$

$$f_{yen}^1 = \frac{1}{l} \int_{-l}^{l} f_y^1(x) \cos \alpha_n x dx, f_{yon}^1 = \frac{1}{l} \int_{-l}^{l} f_y^1(x) \sin \alpha_n x dx, \quad n = 1, 2, \ldots$$

$$f_{ye0}^1 = \frac{1}{2l} \int_{-l}^{l} f_y^1(x) dx$$

$$\tag{A.3}$$

then the coefficients $\{C_0, C_1, C_2, C_3, C_4, C_{30}, C_{40}\}$ and $\{C_{1n}, C_{2n}, C_{3n}, C_{4n}, D_{1n}, D_{2n}, D_{3n}, D_{4n}, n = 1, 2, \ldots\}$ can be expressed in a form explicitly dependent on the boundary loads. Note that in (A.3) subscript $e(o)$ indicates even (odd) coefficients of cosine (sine).

Similar representations hold for (f_y^2, f_x^1, f_x^2). The stress field is therefore completely determined by the Fourier coefficients of $(f_x^1, f_y^1, f_x^2, f_y^2)$ and the constants (N_1, Q_1, M_1). The displacement follows by direct integration of the stress displacement relations obtained from (4) and (6). We record here for reference the boundary displacement components $u_x(x, y = \pm h)$, $u_y(x, y = \pm h)$ which are required in the formulation of the governing equations,

$$u_x(x, y = \varepsilon l) = u_{Rx} - \omega \varepsilon l + h_x(x) + \int_{-l}^{l} K_{xy}^1(x, x') f_y^1(x') dx'$$
$$+ \int_{-l}^{l} K_{xy}^2(x, x') f_y^2(x') dx' + \int_{-l}^{l} K_{xx}^1(x, x') f_x^1(x') dx'$$
$$+ \int_{-l}^{l} K_{xx}^2(x, x') f_x^2(x') dx'$$

$$u_y(x, y = \varepsilon l) = u_{Ry} + \omega x + h_y(x) + \int_{-l}^{l} K_{yy}^1(x, x') f_y^1(x') dx'$$
$$+ \int_{-l}^{l} K_{yy}^2(x, x') f_y^2(x') dx' + \int_{-l}^{l} K_{yx}^1(x, x') f_x^1(x') dx'$$
$$+ \int_{-l}^{l} K_{yx}^2(x, x') f_x^2(x') dx'$$

(A.4)

where the functions (h_x, h_y) depend on the resultant end loadings $(N_1, Q_1, M_1, N_2, Q_2, M_2)$, the material properties, and the thickness ratio ε which is the non-dimensional length ratio h/l. In (A.4) the $(K_{xx}^i, K_{xy}^i, K_{yx}^i, K_{yy}^i)$ are kernel functions with $i = 1, 2$ indicating the particular surface or interface. These quantities are generally dependent on layer elastic properties E, υ, ρ, layer half-length l and thickness ratio ε. Note that the boundary displacement includes rigid body displacement components $u_{Rx} - \omega \varepsilon l$, $u_{Ry} + \omega x$. This is because the sublayer has yet to be fixed in space. Explicit expressions for (h_x, h_y) and the $(K_{xx}^i, K_{xy}^i, K_{yx}^i, K_{yy}^i)$ are not given. Similar quantities for the sublayer system follow. The displacement components at the boundary $y = -h = -\varepsilon l$ can be obtained from (A.4) by replacing ε with $-\varepsilon$.

$$K_{yy}^1(x, x') = \frac{K_n}{l} \cos \alpha_n(x - x') + \frac{P_n}{2l} \cos \alpha_n x + \frac{3}{16}\left(\frac{\beta_{11}}{\varepsilon^3}\frac{x^2}{l^2} - \frac{\beta_{12}}{\varepsilon}\right)\frac{x'^2 l^2}{} + \frac{\beta_{22}\varepsilon}{4}$$

$$K_{yy}^2(x, x') = \frac{L_n}{l} \cos \alpha_n(x - x') - \frac{P_n}{2l} \cos \alpha_n x - \frac{3}{16}\left(\frac{\beta_{11}}{\varepsilon^3}\frac{x^2}{l^2} - \frac{\beta_{12}}{\varepsilon}\right)\frac{x'^2 l^2}{} + \frac{\beta_{22}\varepsilon}{4}$$

$$K_{yx}^1(x, x') = -\frac{M_n}{l} \sin \alpha_n(x - x') - \left(\frac{3\beta_{11}}{8\varepsilon^2}\frac{x^2}{l^2} - \frac{5\beta_{12}}{8}\right)\frac{x'}{l} + \frac{\beta_{66}}{4}\frac{x}{l}$$

$$K_{yx}^2(x, x') = -\frac{N_n}{l} \sin \alpha_n(x - x') - \left(\frac{3\beta_{11}}{8\varepsilon^2}\frac{x^2}{l^2} - \frac{\beta_{12}}{8}\right)\frac{x'}{l} + \frac{\beta_{66}}{4}\frac{x}{l}$$

$$K_{xy}^1(x, x') = -\frac{M_n}{l} \sin \alpha_n(x - x') + \frac{S_n}{2l} \sin \alpha_n x - \frac{3}{8}\frac{\beta_{11}}{\varepsilon^2}\frac{x x'^2}{l l^2} + \frac{\beta_{12}}{4}\frac{x}{l}$$

$$K_{xy}^2(x, x') = -\frac{N_n}{l} \sin \alpha_n(x - x') - \frac{S_n}{2l} \sin \alpha_n x + \frac{3}{8}\frac{\beta_{11}}{\varepsilon^2}\frac{x x'^2}{l l^2} + \frac{\beta_{12}}{4}\frac{x}{l}$$

$$K_{xx}^1(x, x') = \frac{Q_n}{l} \cos \alpha_n(x - x') + \frac{\beta_{11}}{\varepsilon}\frac{x x'}{l l}$$

$$K_{xx}^2(x, x') = \frac{R_n}{l} \cos \alpha_n(x - x') + \frac{\beta_{11}}{2\varepsilon}\frac{x x'}{l l}$$

(A.5)

$$h_y(x) = \left(-\frac{3\beta_{11}x^2}{8l^3\varepsilon^3} + \frac{\beta_{11}x^3}{8l^4\varepsilon^3} + \frac{3\beta_{12}}{8l\varepsilon} - \frac{3x(\beta_{12} + \beta_{66})}{8l^2\varepsilon}\right)M_1$$
$$+ \left(-\frac{3\beta_{11}x^2}{8l^3\varepsilon^3} - \frac{\beta_{11}x^3}{8l^4\varepsilon^3} + \frac{3\beta_{12}}{8l\varepsilon} + \frac{3x(\beta_{12} + \beta_{66})}{8l^2\varepsilon}\right)M_2$$
$$+ \frac{\beta_{12}}{4}\left(1 - \frac{x}{l}\right)N_1 + \frac{\beta_{12}}{4}\left(1 + \frac{x}{l}\right)N_2$$
$$- \left(\frac{3\beta_{11} + 2\varepsilon^2(\beta_{12} + \beta_{66})}{16\varepsilon^3}\frac{x^2}{l^2} - \frac{3\beta_{12} + 2\beta_{22}\varepsilon^2}{16\varepsilon}\right)(Q_1 - Q_2)$$

$$h_x(x) = \left(-\frac{3\beta_{11}x^2}{8l^3\varepsilon^2} + \frac{3\beta_{11}x}{4l^2\varepsilon^2} + \frac{(\beta_{12} + \beta_{66})}{8l}\right)M_1$$
$$+ \left(\frac{3\beta_{11}x^2}{8l^3\varepsilon^2} + \frac{3\beta_{11}x}{4l^2\varepsilon^2} - \frac{(\beta_{12} + \beta_{66})}{8l}\right)M_2$$
$$+ \left(-\frac{\beta_{11}x^2}{8l^2\varepsilon} + \frac{\beta_{11}x}{4l\varepsilon} + \frac{(\beta_{12} + \beta_{66})\varepsilon}{8}\right)N_1$$
$$+ \left(\frac{\beta_{11}x^2}{8l^2\varepsilon} + \frac{\beta_{11}x}{4l\varepsilon} - \frac{(\beta_{12} + \beta_{66})\varepsilon}{8}\right)N_2$$
$$+ \frac{x}{l}\left(\frac{3\beta_{11}}{8\varepsilon^2} + \frac{\beta_{12}}{4}\right)(Q_1 - Q_2)$$

$\rho > 1$:

$$\gamma' = \sqrt{\frac{\rho+1}{2}}/\sqrt[4]{\lambda} \quad \delta = \sqrt{\frac{\rho-1}{2}}/\sqrt[4]{\lambda}$$

$$K_n = \frac{\beta_{22}\gamma'\delta\sqrt{\lambda}(\delta \sinh(4l\alpha_n\gamma'\varepsilon) + \gamma' \sinh(4l\alpha_n\delta\varepsilon))}{\alpha_n(\delta^2 \sinh^2(2l\alpha_n\gamma'\varepsilon) - \gamma'^2 \sinh^2(2l\alpha_n\delta\varepsilon))}$$

$$L_n = -\frac{2\beta_{22}\gamma'\delta\sqrt{\lambda}(\gamma' \cosh(2l\alpha_n\gamma'\varepsilon)\sinh(2l\alpha_n\delta\varepsilon) + \delta \cosh(2l\alpha_n\delta\varepsilon)\sinh(2l\alpha_n\gamma'\varepsilon))}{\alpha_n(\delta^2 \sinh^2(2l\alpha_n\gamma'\varepsilon) - \gamma'^2 \sinh^2(2l\alpha_n\delta\varepsilon))}$$

$$M_n = \frac{-\beta_{22}\rho + \frac{\beta_{12}}{\sqrt{\lambda}} + \delta^2(\beta_{22}\sqrt{\lambda} + \beta_{12})\cosh(4l\alpha_n\gamma'\varepsilon) - \gamma'^2(\beta_{12} - \beta_{22}\sqrt{\lambda})\cosh(4l\alpha_n\delta\varepsilon)}{\alpha_n(\delta^2 \sinh^2(2l\alpha_n\gamma'\varepsilon) - \gamma'^2 \sinh^2(2l\alpha_n\delta\varepsilon))}$$

$$N_n = \frac{2\beta_{22}\gamma'\delta\sqrt{\lambda}\sinh(2l\alpha_n\delta\varepsilon)\sinh(2l\alpha_n\gamma'\varepsilon)}{\alpha_n(\delta^2 \sinh^2(2l\alpha_n\gamma'\varepsilon) - \gamma'^2 \sinh^2(2l\alpha_n\delta\varepsilon))}$$

$$P_n = \frac{(-1)^n(\delta(\beta_{22}\sqrt{\lambda} + \beta_{12})\sinh(2l\alpha_n\gamma'\varepsilon) + \gamma'(\beta_{22}\sqrt{\lambda} - \beta_{12})\sinh(2l\alpha_n\delta\varepsilon))}{l\alpha_n^2\varepsilon(\delta \sinh(2l\alpha_n\gamma'\varepsilon) - \gamma' \sinh(2l\alpha_n\delta\varepsilon))}$$

$$Q_n = -\frac{\beta_{11}\gamma'\delta(\delta \sinh(4l\alpha_n\gamma'\varepsilon) - \gamma' \sinh(4l\alpha_n\delta\varepsilon))}{\alpha_n(\delta^2 \sinh^2(2l\alpha_n\gamma'\varepsilon) - \gamma'^2 \sinh^2(2l\alpha_n\delta\varepsilon))}$$

$$R_n = \frac{2\beta_{11}\gamma'\delta(\gamma' \cosh(2l\alpha_n\gamma'\varepsilon)\sinh(2l\alpha_n\delta\varepsilon) - \delta \cosh(2l\alpha_n\delta\varepsilon)\sinh(2l\alpha_n\gamma'\varepsilon))}{\alpha_n(\delta^2 \sinh^2(2l\alpha_n\gamma'\varepsilon) - \gamma'^2 \sinh^2(2l\alpha_n\delta\varepsilon))}$$

$$S_n = \frac{2(-1)^n\beta_{11}\gamma'\delta(\cosh(2l\alpha_n\gamma'\varepsilon) - \cosh(2l\alpha_n\delta\varepsilon))}{l\alpha_n^2\varepsilon(\delta \sinh(2l\alpha_n\gamma'\varepsilon) - \gamma' \sinh(2l\alpha_n\delta\varepsilon))}$$

$\rho < 1$:

$$\gamma' = \sqrt{\frac{\rho+1}{2}}/\sqrt[4]{\lambda} \quad \delta' = \sqrt{\frac{1-\rho}{2}}/\sqrt[4]{\lambda}$$

$$K_n = \frac{\beta_{22}\gamma'\delta'\sqrt{\lambda}(\delta' \sinh(4l\alpha_n\gamma'\varepsilon) + \gamma' \sin(4l\alpha_n\delta'\varepsilon))}{\alpha_n(\delta'^2 \sinh^2(2l\alpha_n\gamma'\varepsilon) - \gamma'^2 \sin^2(2l\alpha_n\delta'\varepsilon))}$$

$$L_n = -\frac{2\beta_{22}\gamma'\delta'\sqrt{\lambda}(\gamma' \cosh(2l\alpha_n\gamma'\varepsilon)\sin(2l\alpha_n\delta'\varepsilon) + \delta' \cos(2l\alpha_n\delta'\varepsilon)\sinh(2l\alpha_n\gamma'\varepsilon))}{\alpha_n(\delta'^2 \sinh^2(2l\alpha_n\gamma'\varepsilon) - \gamma'^2 \sin^2(2l\alpha_n\delta'\varepsilon))}$$

$$M_n = \frac{\beta_{22}\rho - \frac{\beta_{12}}{\sqrt{\lambda}} + \delta'^2(\beta_{22}\sqrt{\lambda} + \beta_{12})\cosh(4l\alpha_n\gamma'\varepsilon) + \gamma'^2(\beta_{12} - \beta_{22}\sqrt{\lambda})\cos(4l\alpha_n\delta'\varepsilon)}{2\alpha_n(\delta'^2 \sinh^2(2l\alpha_n\gamma'\varepsilon) - \gamma'^2 \sin^2(2l\alpha_n\delta'\varepsilon))}$$

$$N_n = \frac{2\beta_{22}\gamma'\delta'\sqrt{\lambda}\sin(2l\alpha_n\delta'\varepsilon)\sinh(2l\alpha_n\gamma'\varepsilon)}{\alpha_n(\delta'^2 \sinh^2(2l\alpha_n\gamma'\varepsilon) - \gamma'^2 \sin^2(2l\alpha_n\delta'\varepsilon))}$$

$$P_n = \frac{(-1)^n(\delta'(\beta_{22}\sqrt{\lambda} + \beta_{12})\sinh(2l\alpha_n\gamma'\varepsilon) + \gamma'(\beta_{22}\sqrt{\lambda} - \beta_{12})\sin(2l\alpha_n\delta'\varepsilon))}{l\alpha_n^2\varepsilon(\delta' \sinh(2l\alpha_n\gamma'\varepsilon) - \gamma' \sin(2l\alpha_n\delta'\varepsilon))}$$

$$Q_n = \frac{\beta_{11}\gamma'\delta'(\delta' \sinh(4l\alpha_n\gamma'\varepsilon) - \gamma' \sin(4l\alpha_n\delta'\varepsilon))}{\alpha_n(\delta'^2 \sinh^2(2l\alpha_n\gamma'\varepsilon) - \gamma'^2 \sin^2(2l\alpha_n\delta'\varepsilon))}$$

$$R_n = \frac{2\beta_{11}\gamma'\delta'(\gamma' \cosh(2l\alpha_n\gamma'\varepsilon)\sin(2l\alpha_n\delta'\varepsilon) - \delta' \cos(2l\alpha_n\delta'\varepsilon)\sinh(2l\alpha_n\gamma'\varepsilon))}{\alpha_n(\delta'^2 \sinh^2(2l\alpha_n\gamma'\varepsilon) - \gamma'^2 \sin^2(2l\alpha_n\delta'\varepsilon))}$$

$$S_n = \frac{2(-1)^n\beta_{11}\gamma'\delta'(\cosh(2l\alpha_n\gamma'\varepsilon) - \cos(2l\alpha_n\delta'\varepsilon))}{l\alpha_n^2\varepsilon(\delta' \sinh(2l\alpha_n\gamma'\varepsilon) - \gamma' \sin(2l\alpha_n\delta'\varepsilon))}$$

References

Au, C., Buyukozturk, O., 2006. Debonding of FRP plated concrete: a tri-layer fracture treatment. Engineering Fracture Mechanics 73, 348–365.

Bao, G., Ho, S., Suo, Z., Fan, B., 1992. The role of material orthotropy in fracture specimens for composites. Int J Solids Structures 29 (9), 1105–1116.

Boelen, B., den Hartog, H., van der Weijde, H., 2004. Product performance of polymer coated packaging steel, study of the mechanism of defect growth in cans. Progress in Organic Coatings 50, 40–46.

Carpinteri, A., Lacidogna, G., Paggi, M., 2007. Acoustic emission monitoring and numerical modeling of FRP delamination in RC beams with non-rectangular cross-section. Materials and Structures 40, 553–566.

Chvedov, D., Jones, R., 2004. Frictional behavior of rolled surfaces coated with polymer films. Surface Coating Technology 188–189, 544–549.

Corless, R.M., Gonnet, G.H., Hare, D.E.G., Jeffrey, D.J., Knuth, D.E., 1996. On the Lambert W function. Advances in Computational Mathematics 5 (1), 329–359.

Ferrante, J., Smith, J.R., Rose, J.H., 1982. Universal binding energy relations in metallic adhesion. Microscopic aspects of adhesion and lubrication, in: Proceedings of the 34th international meeting of the societe de chimie physique. Paris, Fr, Elsevier Scientific Publication Company.

Graziano, F., 2000. Coil and sheet coating. Metal Finishing 98, 175–176.

Koiter, W.T., Benthem, J.P., 1973. In: G.C. Sih (ed.), Mechanics of Fracture, Noordhoff, Leyden 1, 131–178.

Krenk, S., 1979. On the elastic constants of plane orthotropic elasticity. Journal of Composite Materials 13, 108–116.

Lekhnitskii, S.G., 1981. Theory of elasticity of an anisotropic body. Mir, Moscow.

Needleman, A., 1990a. An analysis of tensile decohesion along an imperfect interface. International Journal of Fracture 42, 21–40.

Needleman, A., 1990b. An analysis of tensile decohesion along an Interface. Journal of the Mechanics and Physics of Solids 38, 289–324.

Nguyen, C.M., Levy, A.J., 2009. An exact theory of interfacial debonding in layered elastic composites. International Journal of Solids Structures 46 (13), 2712–2723.

Nguyen, C.M., Levy, A.J., 2011. Mechanics of interface failure in the trilayer elastic composite. International Journal of Solids Structures 48 (13), 2467–2484.

Niu, X., Yang, Y., Soboyejo, W., 2008. Contact deformation and cracking of zirconia/cement/foundation dental multilayers. Materials Science and Engineering A485, 517–523.

Pan, J., Leung, C.K.Y., 2007. Debonding along the FRP-concrete interface under combined pulling/peeling effects. Engineering Fracture Mechanics 74, 132–150.

Rabinovitch, O., 2008. Cohesive interface modeling of debonding failure in FRP strengthened beams. Journal of Engineering Mechanics 134, 578–588.

Raous, M., 2011. Interface models coupling adhesion and friction. Comptes Rendus Mecanique 339 (7–8), 491–501.

Suo, Z., 1990. Delamination specimens for orthotropic materials. Journal of Applied Mechanics 57, 627–634.

Suo, Z., Bao, G., Fan, B., Wang, T.C., 1991. Orthotropy rescaling and implications for fracture in composites. International Journal of Solids Structures 28 (2), 235–248.

Van den Bosch, M.J., Schreurs, P.J.G., Geers, M.G.D., 2006. An improved description of the exponential Xu and Needleman cohesive zone law for mixed-mode decohesion. Engineering Fracture Mechanics 73, 1220–1234.

Wang, J., 2007. Cohesive zone model of FRP-concrete interface debonding under mixed-mode loading. International Journal of Solids and Structures 44, 6551–6568.

Xu, X., Needleman, A., 1993. Void nucleation by inclusion debonding in a crystal matrix. Modeling and Simulation in Materials Science and Engineering 1 (2), 111–132.